Structure-based insights into the mechanism of [4Fe-4S]-dependent sulfur insertase LarE

Paolo Zecchin, Ludovic Pecqueur, Jonathan Oltmanns, Christophe Velours, Volker Schünemann, Marc Fontecave, Béatrice Golinelli-Pimpaneau

Structure-based insights into the mechanism of [4Fe-4S]-dependent sulfur insertase LarE

Paolo Zecchin[1], Ludovic Pecqueur[1], Jonathan Oltmanns[2], Christophe Velours[3,4], Volker Schünemann[2], Marc Fontecave[1], Béatrice Golinelli-Pimpaneau[1]*

[1] Laboratoire de Chimie des Processus Biologiques, Collège de France, CNRS UMR 8829, Sorbonne Université, 11 Place Marcelin Berthelot, 75231 Paris cedex 05, France

[2] Universität of Kaiserslautern-Landau, Department of Physics, Erwin-Schrödinger-Str. 46, D-67663 Kaiserslautern, Germany

[3] Institute for Integrative Biology of the Cell (I2BC), CEA, CNRS, Université Paris-Saclay, Avenue de la Terrasse, 91198 Gif-sur-Yvette cedex, France

[4] Present address: Fundamental Microbiology and Pathogenicity Laboratory, UMR 5234 CNRS-University of Bordeaux, SFR TransBioMed. Bordeaux, France

* corresponding author: beatrice.golinelli@college-de-france.fr, tel: +33 1 44 27 12 52, fax: +33 1 44 27 14 83

Abstract

Several essential cellular metabolites, such as enzyme cofactors, contain sulfur atoms and their biosynthesis requires specific thiolation enzymes. LarE is an ATP-dependent sulfur insertase, which catalyzes the sequential conversion of the two carboxylate groups of the precursor of the lactate racemase cofactor into thiocarboxylates. Two types of LarE enzymes are known, one that uses a catalytic cysteine as a sacrificial sulfur donor, and the other one that uses a [4Fe-4S] cluster as a cofactor. Only the crystal structure of LarE from *Lactobacillus plantarum* (LpLarE) from the first class has been solved. We report here the crystal structure of LarE from *Methanococcus maripaludis* (MmLarE), belonging to the second class, in the cluster-free (apo-) and cluster-bound (holo-) forms. The structure of holo-MmLarE shows that the [4Fe-4S] cluster is chelated by three cysteines only, leaving an open coordination site on one Fe atom. Moreover, the fourth non-protein-bonded iron atom was able to bind an anionic ligand such as a phosphate group or a chloride ion. Together with the spectroscopic analysis of holo-MmLarE and the previously reported biochemical investigations of holo-LarE from *Thermotoga maritima*, these crystal structures support the hypothesis of a reaction mechanism, in which the [4Fe-

4S] cluster binds a hydrogenosulfide ligand in place of the chloride anion, thus generating a [4Fe-5S] intermediate, and transfers it to the substrate, as in the case of [4Fe-4S]-dependent tRNA thiolation enzymes.

Keywords sulfur insertase; LarE; iron sulfur cluster, [4Fe-4S]; [4Fe-5S]; crystal structure; catalytic mechanism; AlphaFold

running title: crystal structure of [4Fe-4S]-dependent LarE

22 manuscript pages, 15 supplementary material pages, 1 table, and 7 figures

Supplementary material

Broad audience statement

LarE enzymes insert two sulfur atoms within the cofactor of lactate racemase using two distinct catalytic mechanisms. In contrast to LpLarE, which sacrifices the sulfur atom of one cysteine, MmLarE uses a [4Fe-4S] cluster as a cofactor for the sulfuration reaction. The crystal structure of holo-MmLarE shows that the [4Fe-4S] cluster, bound to three cysteines only, can bind a chloride ion. A [4Fe-5S] intermediate is likely the sulfur donor in the MmLarE-catalyzed reaction

1 Introduction

Lactate racemase (LarA) interconverts the D- and L- isomers of lactic acid, a central metabolite in many organisms. Lactic acid is involved in the energy metabolism of many prokaryotes, as a product of sugar fermentation or as a carbon and electron source to sustain growth. Lactate racemization is a rescue pathway for supplying D-lactate to the cell wall biosynthesis machineries in bacteria such as *Lactobacillus plantarum* (Goffin et al. 2005). The LarA enzyme depends on an organometallic cofactor named nickel-pincer nucleotide (NPN) (Figure 1), which is bound to conserved histidines through the Ni center (Desguin et al. 2014) . The synthesis of NPN requires three enzymes (Figure 1). LarB converts nicotinic acid dinucleotide (NaAD) into pyrimidinium-3,5-biscarboxylic acid mononucleotide (P2CMN) and adenosine monophosphate (AMP) by carboxylating the C5 atom of the pyridinium ring using bicarbonate. Then, adenosine triphosphate (ATP)-dependent sulfur insertase LarE sequentially converts the two carboxylate groups of P2CMN into thiocarboxylates to yield first pyridinium-3-carboxy-5-thiocarboxylic acid mononucleotide (PCTMN) and then pyridinium-3,5-bisthiocarboxylic acid mononucleotide (P2TMN). Finally, cytidine triphosphate (CTP)-dependent LarC inserts nickel into P2TMN to yield NPN.

LarE enzymes belong to the N-type pyrophosphate (PP)-loop proteins superfamily and share a common pyrophosphatase (PPase) catalytic domain (Fellner et al. 2018a) (Figure S1). Two distinct classes of LarE proteins, operating with different catalytic mechanisms, have been described. In the first class, exemplified by LarE from *L. plantarum* (LpLarE), one conserved cysteine, Cys176, sacrifices its sulfur atom to give it for insertion into P2CMN, being thus converted into dehydroalanine (Fellner et al. 2017). In contrast, the major class, exemplified by LarE from *Thermotoga maritima* (TmLarE), contains a CXXC + C motif. It was proposed that the cysteines of this motif bind a [4Fe-4S] cluster that is essential for catalysis, based on activity tests of TmLarE, the Electron Paramagnetic Resonance (EPR) spectrum of the reduced wild-type enzyme and the characterization of the triple cysteine to alanine mutant, which was shown to contain almost no cluster and was nearly catalytically inactive (Chatterjee et al. 2022). Moreover, it was shown that the catalytic activity of holo-TmLarE was increased four-fold by incubation with L-cysteine and cysteine desulfurase IscS, an enzyme system that liberates sulfur from L-cysteine in the form of a IscS-bound persulfide. Finally, electrospray ionization mass spectrometry (ESI-MS) analysis indicated that the sulfane atom of the IscS-bound persulfide is lost upon incubation with holo-TmLarE. These results suggested that the sulfane atom can be transferred to the cluster of TmLarE to form a [4Fe-5S] species, catalytically competent to give a sulfur atom to the PCMN substrate (Chatterjee et al. 2022).

Whereas the crystal structure of sacrificial LpLarE has been solved (Fellner et al. 2017), the structure of [4Fe-4S]-dependent LarE proteins has not been determined experimentally. In order to decipher how two enzymes are able to catalyze the same reaction using two different kinds of catalytic mechanisms, we report here the crystal structure of LarE from *Methanococcus maripaludis* (MmLarE; 28.3%

sequence identity with TmLarE), which, like TmLarE, is a [4Fe-4S]-dependent protein. Comparison of the structures of apo-MmLarE (without the cluster) and holo-MmLarE (with bound cluster) suggests that the cluster, in addition to its catalytic function, fulfills a structural role by stabilizing the folding of the two domains of LarE (C-terminal and P2CMN-binding domains) into a catalytically competent conformation. One of the holo-MmLarE structures shows that a chloride ion can serve as a ligand of one Fe atom of the [4Fe-4S cluster], while the three other Fe atoms are coordinated by conserved cysteines. This illustrates the ability of the cluster to bind an exogenous inorganic anion and provides a model for the [4Fe-5S] cluster intermediate proposed as the S atom donor during catalysis. Based on the various crystal structures of LpLarE and MmLarE, we modeled various catalytic intermediates along the MmLarE- and Lp-LarE-catalyzed sulfur-insertion reaction. These models, together with the comparison of the active site structures of the two types of LarE enzymes, gives insights into their distinct catalytic mechanism.

2 Results

2.1 Purification and characterization of MmLarE

MmLarE was expressed with a cleavable N-terminal 6-histidine tag, then purified under aerobic conditions by nickel affinity chromatography (Figure S2A). The tag was removed using the H3C protease and the protein was further purified by size-exclusion chromatography (Figures S2B and S2C, first column). The protein purified this way, named 'as-purified' MmLarE, appeared colorless and exhibited a UV-visible spectrum with no absorption band at around 410 nm, indicating that the protein is devoid of [Fe-S] clusters **(**Figure 2A). This result was confirmed by the quantification of Fe using the Fish method, which uses permanganate to release the complexed iron in solution, ascorbic acid to reduce it, and ferrozine and neocuproine to chelate it, the formation of the [Fe^{II}]ferrozine complex being quantified by absorption colorimetry (Fish 1988). The Fe content was less than 0.1 ± 0.2 mole Fe per monomer.

2.2 A [4Fe-4S] cluster can be assembled in MmLarE

Cluster reconstitution was carried out, under strict anaerobic conditions, by treating the 'as-purified' protein with a 5-molar excess of ferrous iron in the presence of a sulfur source (consisting in L-cysteine and cysteine desulfurase CsdA), and a reductant (dithiothreitol, DTT). The protein was then purified on a Superdex 200 gel filtration column (Figure S3A), also under anaerobic conditions, leading to a homogenous brownish protein containing a [Fe-S] cluster that was subsequently called holo-MmLarE. Size Exclusion Chromatography coupled with Multi-Angle Light Scattering (SEC-MALS) analysis of holo-MmLarE indicated that it was a dimer in solution (measured molar mass of 58.8 ± 0.6 kDa; theoretical molar mass of one monomer: 31,12 kDa) (Figure S3B).

Quantification of the iron content in holo-MmLarE gave 3.1 ± 0.2 Fe per monomer. The UV-visible spectrum of purified holo-MmLarE displayed a broad absorption band at around 410 nm that is characteristic for the presence of a [4Fe-4S] cluster (Figure 2A). Since Mössbauer spectroscopy using the ^{57}Fe nucleus (Gütlich et al. 2011) is an excellent tool to identify and explore iron-sulfur clusters (Beinert et al. 1997 ; Ueda et al. 2021), we prepared samples with isotopically enriched ^{57}Fe. The Mössbauer spectrum of holo-MmLarE obtained at $T = 77$ K showed a major component (97%), exhibiting a doublet with an isomer shift of $\delta = 0.43$ mm.s^{-1} and a quadrupole splitting of $\Delta E_Q = 1.14$ mm.s^{-1} (Figure 2B, Table S1). These parameters are typical for diamagnetic [4Fe-4S]$^{2+}$ clusters (Schünemann 2021). The observed $\delta = 0.43$ mms^{-1} lies in between the isomer shift values of tetrahedral sulfur-coordinated Fe(II) and Fe(III) and is characteristic for mixed valence Fe(II)Fe(III) pairs with a delocalized electron occurring twice in diamagnetic [4Fe-4S]$^{2+}$ clusters. The minor component (3%), with $\delta = 1.13$ mm.s^{-1} and $\Delta E_Q = 2.69$ mm.s^{-1} is characteristic of high spin Fe^{2+} (Schünemann et al. 1999). The diamagnetic ground state of the [4Fe-4S]$^{2+}$ cluster was confirmed by a Mössbauer spectrum recorded at $T = 4.2$ K and an applied magnetic field $B_{ext} = 5.0$ T. This spectrum shows magnetic splitting, which is due to the external field only, and could be simulated, assuming a diamagnetic ground state of the [4Fe-4S]$^{2+}$ cluster, using the spin Hamiltonian formalism (Gütlich et al. 2011) (Pandelia et al. 2015)(Figure S4 and Table S1). Since no further components could be identified, our Mössbauer spectroscopy analysis confirmed the absence of other clusters such as [2Fe-2S]$^{2+}$ and [3Fe-4S]$^{+}$ clusters (Pandelia et al. 2015).

2.3 Determination of the crystal structure of holo-MmLarE using SAD-phasing

We initially obtained crystals of holo-MmLarE diffracting at 3.2 Å resolution, which belonged to space group $C222_1$ (Crystal 1, Table 1). Since the AlphaFold software (Jumper et al. 2021), which accurately predicts the three-dimensional structure of proteins based on their sequence only, was not released at that time, we first attempted to phase the data by molecular replacement with *PHASER* (McCoy et al. 2007). LpLarE was used as a model (PDB code 5UDQ; 26.8% sequence identity with MmLarE; see sequence alignment in Figure S1), after editing the coordinates with *SCULPTOR* (Bunkóczi and Read 2011). However, the search for the full model or two domains failed. As MmLarE contains a [4Fe-4S] cluster, the structure was solved by single anomalous diffusion (SAD) using data collected at the Fe edge (7.125 keV, Table 1). The experimental map contained an anomalous signal up to 4.5 Å resolution, which allowed to build a model with seven copies in the asymmetric unit after a laborious sequence of steps (see section 4.2). This first holo-MmLarE crystal structure was refined at 3.6 Å resolution.

The asymmetric unit is composed of seven monomers (Figure 3A), among which six form dimers (Figure 3B). The seventh monomer also forms a dimer with another monomer from the neighboring asymmetric unit. This is consistent with the observation that MmLarE is a homodimer in solution, as shown by SEC-MALS analysis (Figure S3B). The crystal packing involves heptamers of dimers (Figure S5), the interface of the most tightly assembled dimer being 907 ±14 Å^2 and the interface of the others

being 456 ± 42 Å^2 and 231 ± 19 Å^{2,} as calculated with PISA (Krissinel 2010). Thus, the analysis of the crystallographic contacts supports that the enzyme is functional as a dimer, in agreement with the analysis of the oligomeric state in solution. The seven chains of the holo-MmLarE crystal structure are very close to each other (Figure 3C and Table S2).

One monomer, composed of 13 α-helices and 7 β-strands, can be decomposed into two domains, the N-terminal catalytic domain (residues M1-L164) and the C-terminal domain (residues M175-K258) (Figure 3B). Like in LpLarE, the N-terminal domain contains the characteristic PP-loop motif for ATP binding (SGGxDS (Fellner et al. 2017); see Figure S1). It also contains two of the three cysteines involved in coordination of the iron-sulfur cluster of MmLarE (see below). Dimerization occurs through the C-terminal end (residues M214-K258) (Figure 3B and 3D), which includes an antiparallel β-sheet between strand β7 (residues V251-L255) from each chain, as well as numerous van der Waals interactions and a few electrostatic interactions. A linker (residues K165-C174) connects the two domains and contains the last cysteine used in iron-sulfur cluster coordination (see below). Thus, the [4Fe-4S] cluster is bound at the interface between the N- and C-terminal domains (Figures 3B and 3C).

2.4 The *AlphaFold2* model of MmLarE exhibits a globular architecture ready to bind the cluster

During the course of this study, the *AlphaFold* software was released (Jumper et al. 2021). The superposition of each chain of the holo-MmLarE crystal structure with the *AlphaFold2* model (AF-Q6LXV7-F1-model_v4) using the program *ProFit3* (http://www.bioinf.org.uk/software/profit) gives an average root mean square deviation (RMSD) of 0.57 - 0.87 Å for 248 Cα atoms (Figure S6 and Table S2). This indicates that the *AlphaFold2* model is very close to the experimentally determined crystal structure of the holo-enzyme. Interestingly, the prediction by AlphaFold2, which did not contain any information about the cluster, gives a model of the MmLarE monomer with a globular fold, in which the three cysteines expected to coordinate the cluster adopt a geometry compatible with cluster binding. This result was also reported for several other [Fe-S]-binding proteins (Golinelli-Pimpaneau 2022).

In addition, the *AlphaFold2* model of the MmLarE dimer was calculated, and was predicted with a high confidence (Predicted Local-Distance Difference Test of 91.1 and predicted Template Modeling score of 0.82) (Figure S6C). Again, the model of the dimer is very close to the structure obtained from the experimental crystallographic data of the holo-enzyme. However, after superimposition of one monomer from the *AlphaFold2* model and the crystal structure (RMSD of 0.989 Å over 1765 Cα atoms), the orientation of the second monomer relative to the first monomer is different (Figure S6C), showing flexibility of one monomer relative to the other. The conformation adopted by the two monomers in the crystal was not predicted by *AlphaFold2*.

2.5 In holo-MmLarE, the [4Fe-4S] cluster is chelated by three conserved cysteines only and the fourth nonprotein bonded Fe atom is able to bind a negatively charged ligand

A more complete data set of holo-MmLarE was then obtained on another crystal (Crystal 2, Table 1), and the structure was refined at 3.2 Å resolution using the previous model of holo-MmLarE obtained by SAD phasing. In each monomer, one [4Fe-4S] cluster, refined with an occupancy of 0.9-1.0, was bound between the N-terminal and C-terminal domains. It is chelated to the protein by the three conserved cysteines Cys96, Cys99, and Cys174 (Figure 4A). Surprisingly, in one of the molecules in the asymmetric unit (A), an electron density near the fourth iron atom of the cluster revealed the presence of a molecule such as a nucleotide, likely coordinated to it (Figure 4B). To identify this molecule, the 'as-purified' protein was precipitated by acidic treatment, neutralized and the supernatant was analyzed by reversed-phase High Performance Liquid Chromatography (HPLC) (Figure S7A). By comparison with AMP and ATP standards, the released nucleotide was identified as AMP, one of the products of the reaction, which likely remained bound to the protein throughout the purification procedure. Nucleotide quantification in the 'as-purified' protein by HPLC gave a 12.5 ± 1.4 % mole per mole ratio of AMP to 'as-purified' MmLarE. AMP fitted the electron density present in molecule A near the [4Fe-4S] cluster, and was refined with an occupancy of 80% (Figure 4B). Two oxygens of the AMP phosphate group lied 2.5Å and 2.9 Å away from the non-protein bonded Fe atom of the cluster, completing its coordination. In the six other molecules in the asymmetric unit, three Fe atoms of the cluster were attached to the protein via the three conserved cysteines, whereas the fourth iron atom was coordinated by a non-protein, small exogenous ligand, as revealed by the observed electron density adjacent to that Fe atom (Figure 4C). Given that the crystals were obtained in the presence of 4.1 M NaCl, this density was assigned to a chloride ion, 2.2 Å away from that Fe atom, which could be refined with a B-factor in the same range as that of the protein. Therefore, in all molecules of the holo-MmLarE crystal structure, a negatively charged group (phosphate group or chloride ion) binds to the fourth iron atom, complementing the positive charge of the $[4Fe\text{-}4S]^{2+}$ cluster.

2.6 The relative position of the two domains of MmLarE is variable

We also obtained crystals of 'as-purified' MmLarE in crystallization conditions different from that of holo-LarE, with ammonium sulfate as the precipitant. The crystals belonged to space group H3, contained two molecules in the asymmetric unit, and diffracted to 2.35 Å resolution (Table 1). Surprisingly, the structure could not be solved simply by molecular replacement using the refined model of holo-MmLarE. The C-terminal and N-terminal domains could be positioned only separately. The search with *PHASER* (McCoy et al. 2007) gave only the position of the N-terminal domains, which were partially refined. Then, the C-terminal domains were positioned with the Spherically Averaged Phased Translation Function (SAPTF) function in *MOLREP* (Vagin and Isupov 2001). The structure, which does not contain any iron-sulfur cluster is named apo-MmLarE.

Actually, the orientation of the N-terminal and C-terminal domains relative to each other are completely different in the apo- and holo-structures (Figures 5A, B and C), which explains why the positioning of the full-length models of holo-MmLarE by molecular replacement failed. Moreover, in the apo-

MmLarE crystal structure, the position of the two domains relative to each other differs in the two molecules in the asymmetric unit (Figure 5A and B). In fact, this particular arrangement, which destroys the dimeric contacts involving the C-terminal end in holo-MmLarE (Figure 5C), is stabilized by a disulfide bond between Cys174 and Cys96 from each monomer linking the two molecules (Figure 5D), despite the presence of a reductant (5 mM β-mercaptoethanol) in the buffer used to purify and store the enzyme. The presence of the disulfide bond was confirmed in solution by nano Liquid Chromatography Mass Spectrometry (nano LC-MS) analysis, which gave a molar mass for apo-MmLarE of 60,829 ± 2 Da, corresponding to the dimeric form (theoretical molar mass of monomer of 31,12 kDa) lacking the last six amino acids (Figure S7B). We noticed that the conformation of the two domains constrained by a disulfide bond in the apo-MmLarE was not predicted by *AlphaFold2*.

The nonhydrolyzable ATP analog, adenylyl-imidodiphosphate (AMP-PNP), which was used in co-crystallization, was observed in the active site, with two alternative conformations of the γ-phosphate (Figure 5E). Comparison of the B-factors of the residues from the N-terminal and C-terminal domains in apo-MmLarE shows that the residues from the N-terminal domains have much lower B-factors (mean value of 80.1 $Å^2$ and 82.4 $Å^2$, for molecules A and B, respectively), than the C-terminal residues (mean value of 146.7 $Å^2$ and 171.8 $Å^2$, for molecules A and B, respectively), which are not involved in dimerization in apo-MmLarE (Figure S8A). This indicates a high disorder within the crystal of the C-terminal domains, which are not involved in dimeric contacts as observed for holo-MmLarE (Figure 3B). The regions in the C-terminal domains of apo-MmLarE, which are not constrained by crystal contacts (Figure S8B), have a poor electron density so that the side chains of the residues are not well-defined. In contrast to apo-MmLarE, the residues from the N- and C-terminal domains of holo-MmLarE had similar B-factors (mean value of 102.7 Å) (Figure S8C).

2.7 Comparison of the holo-MmLarE and LpLarE crystal structures

Superposition of the N-terminal catalytic domains of holo-MmLarE in complex with AMP and LpLarE in complex with nicotinamide mononucleotide (NMN), an analogue of the P2CMN substrate, in which one carboxylate is replaced by an amide group and the second carboxylate is absent (Figure S9), shows that the two proteins adopt the same fold and are structurally similar (Figure 6A). But it also highlights different relative orientations of the N- and C-terminal domains in both crystal structures, likely reflecting a different oligomeric state in solution, dimeric for holo-MmLarE and hexameric for LpLarE (Fellner et al. 2017). This confirms the flexibility of the N-and C-terminal domains relative to each other.

The electrostatic surfaces of holo-MmLarE and LpLarE are very similar, displaying highly positive pockets to bind the phosphate groups of AMP/ATP and that of the substrate (Figure 6C), formed by conserved residues (Figure 6D). A non-conserved region surrounding the binding pocket of LpLarE (G207-V211 and P225-A227; red circle in Figure 6C) is more positive in LpLarE than in MmLarE. The adenine ring of AMP/ATP/AMP-PNP stacks with Ser29, and the hydroxyl groups of the ribose form H-

bonds with the NH group of Gly122 (MmLarE numbering) (Figure S10). The α-phosphate of AMP-PNP is bound by the Nε atom of Lys100 in MmLarE. Like in other PP-loop pyrophosphatases, the PP-loop motif (residues 29-34 in MmLarE, Figure S1) is involved in binding the γ-group of the ATP cofactor, as shown in the apo-MmLarE/AMP-PNP and LpLarE/ATP complexes (Figure S10). In addition, the 'RPG'-containing loop (corresponding to residues 132-134 in MmLarE), characteristic of LarE proteins, is involved in nucleotide binding. Interestingly, in LpLarE, this loop was shown to get ordered upon AMP binding (Fellner et al. 2017). Whereas AMP-PNP in apo-MmLarE and ATP in LpLarE are nearly superimposable, with the equivalent residues being used for nucleotide binding (Figures S10A and S10B), AMP in holo-MmLarE and in LpLarE displays different conformations (Figure S10A and S10C), likely because the phosphate group of AMP is bound to the [4Fe-4S] cluster in holo-MmLarE.

The comparison of the binding sites of holo-MmLarE and LpLarE highlights also similar positioning of the conserved residues Arg210 and Arg212 (Figure S1 and Figure 6B). Since these residues are involved in the binding of the phosphate group of the substrate analog in the crystal structure of LpLarE in complex with NMN (Figure 6B) or a phosphate ion occupying the same position in the LpLarE/ATP complex, the equivalent residues are also likely involved in the binding of the phosphate group of the P2CMN substrate in MmLarE.

Interestingly, one of the cysteines (Cys174), which ligates the [4Fe-4S] cluster in MmLarE, occupies a position similar to that of sacrificial Cys176 of LpLarE (their Cα atoms are 1.7 Å away in the superposition), whereas another cysteine ligand (Cys96) in MmLarE occupies the site of Trp97 in LpLarE (Figure 6B), an invariant residue within the LarE enzymes belonging to the class of sacrificial LpLarE proteins (Figure S1). Furthermore, Trp97 adopts different conformations in the various chains of the LpLarE crystal structure in complex with NMN. In both of them, Trp97 stacks against the nicotinamide ring of the substrate analog, indicating that it serves to stabilize a reactive conformation of the substrate (Figure 6B).

2.8 Models of catalytic intermediates along the LarE-catalyzed reaction

A catalytic mechanism used by [Fe-S]-dependent LarE enzymes, involving the formation of an adenylated intermediate and a [4Fe-5S] cluster, was proposed by Chatterjee et al. (Chatterjee et al. 2022) based on their spectroscopic and biochemical characterization of TmLarE (Figure 7A), extending to LarE a mechanism we previously proposed for sulfuration of tRNAs catalyzed by [4Fe-4S] enzymes such as TtuA (Arragain et al. 2017), TtcA (Bouvier et al. 2014) and NcsA (Bimai et al. 2023). To visualize the different steps in catalysis, the main catalytic intermediates along the reaction were modeled (Figure S11, see details in section 4.9). First, a model of holo-MmLarE bound to the PC2MN substrate and ATP was built (Figure S11A), based on the superposition of the structures of holo-MmLarE with chloride bound to the cluster (molecule B), apo-MmLarE in complex with AMP-PNP

and LpLarE in complex with NMN or ATP (Figure 7B). NMN was then replaced in *COOT* by P2CMN, and a [4Fe-5S] cluster was built by substituting the chloride ion by a hydrogenosulfide ion. This initial complex (Figure S11) was energy-minimized with *PHENIX*. Next, a model of adenylated intermediate I bound to holo-MmLarE was built by bringing the P2CMN molecule into proximity with ATP (while maintaining ATP anchored by the PP-loop) using *COOT* to form a covalent bond between the oxygen atom of one the carboxylic groups of P2CMN and the α phosphorus atom of ATP (Figure S11B). A model of the tetrahedral adenylated intermediate II bound to holo-MmLarE, after transfer of the sulfur atom from the [4Fe-5S] cluster, and a model of the first product complex, containing AMP and P2TMN, were also built (Figure S11B).

The same procedure was performed to model the main intermediates along the LpLarE-catalyzed reaction (Figure S12) to finely compare the active sites of the MmLarE and LpLarE enzymes during catalysis and obtain hints about the different catalytic mechanisms used. First, some differences are observed in the residues involved in the binding of the ribose hydroxyl groups of the substrate: whereas Tyr184, from the conserved motif RXPYG (Figures S1 and S13) of LpLarE, binds the two hydroxyl groups of the P2CMN ribose (Figure S12), this function is fulfilled by Arg95 in MmLarE (Figure S11B), which does not possess the conserved motif. The position of Arg95 in MmLarE corresponds to that of one the conformers of Trp97 in LpLarE, which stabilizes the nicotinamide substrate via stacking interactions.

Second, the two adenylated intermediates are stabilized by the equivalent conserved residues in MmLarE and LpLarE: Lys100 in MmLarE (Lys101 in LpLarE) (Figure S1 and S13) that forms hydrogen bonds with both adenylated intermediates, but not with ATP or AMP, when bound to the PCMN substrate, and Arg132 in MmLarE (Arg133 in LpLarE) that interacts with the α phosphate group of ATP/AMP and brings together the P2CMN substrate and ATP to create a covalent bond linking them and form the adenylated intermediates.

3 Discussion

3.1 Sulfur insertases use various catalytic mechanisms

Sulfur, an essential element for a variety of cellular constituents in all living organisms, is present in several cofactors, vitamins and thionucleosides within tRNA (Shigi 2018; Shigi 2021). The enzymes involved in the biosynthesis of these thio-molecules display a large array of catalytic mechanisms (Chatterjee and Hausinger 2022). Whereas the biosynthesis of lipoic acid, biotin and ms^2i^6A37-tRNA requires S-adenosyl-L-methionine-radical enzymes to insert sulfur within an unactivated C-H bond (Fontecave et al. 2003; Cicchillo et al. 2004; Fugate and Jarrett 2012; Forouhar et al. 2013), the enzymes that catalyze the non-redox substitution of an oxygen atom by a sulfur atom (Bimai et al. 2020), like LarE, display a PP-loop motif characteristic of an ATP binding site, and activation of the target atom by ATP occurs through the formation of a catalytically competent adenylated intermediate. Although all

ATP-dependent sulfur-inserting enzymes possess at least one conserved cysteine that plays a role in catalysis, they were shown to use various catalytic strategies. For example, U8-tRNA sulfurase from *Escherichia coli* possesses a second catalytic cysteine within a rhodanese domain, which serves to form a catalytic persulfide, whereas the conserved cysteine is used as a nucleophile to break a disulfide bond formed during the reaction (Mueller et al. 2001). Several other tRNA thiolation enzymes were shown to bind a [4Fe-4S] cluster, bound by three conserved cysteines, with the fourth nonprotein-bonded Fe atom being capable of binding a hydrogenosulfide ion, which is used as the sulfur donor. Among them, several enzymes (MnmA and NcsA operating on C2 of U34 (Shigi et al. 2020; Zhou et al. 2021a; Bimai et al. 2023), TtuI on C4 of U8 (He et al. 2022) and TtuA on C2 of U54 (Arragain et al. 2017; Chen et al. 2017; Chen et al. 2020; Zhou et al. 2022) have been recently biochemically and/or structurally characterized (Bimai et al. 2020; Shigi 2021). Finally, LpLarE sacrifices its conserved cysteine, which is used as the sulfur donor (Fellner et al. 2017). The crystal structure of LpLarE (Fellner et al. 2017) was the only known crystal structure of a LarE enzyme up to now.

3.2 A [4Fe-5S] catalytic intermediate likely serves as a sulfur donor in [4Fe-4S]-dependent LarE enzymes

We report here the first crystal structures of a [4Fe-4S]-dependent LarE enzyme. The structure of holo-MmLarE revealed the presence of a [4Fe-4S] cluster, bound at the interface between the N-terminal and C-terminal domains, which is chelated to the protein by only three cysteine ligands, leaving a free coordination site on one iron atom. Interestingly, an AMP molecule, inadvertently bound in one of the molecules in the asymmetric unit, indicated that the [4Fe-4S] cluster is located in the catalytic site, in proximity to the ATP binding site. Similarly, an AMP molecule, which appeared to have copurified with the protein, has previously been observed in the crystal structure of the [4Fe-4S]-dependent U54-tRNA thiolation enzyme TtuA (Arragain et al. 2017). Moreover, in the other molecules in the asymmetric unit, the [4Fe-4S] was bound to a smaller ligand, which was assigned to a chloride ion coming from the crystallization solution. A chloride-bound [4Fe-4S] cluster has also been observed in the crystal structure of quinolate synthase, which catalyzes a [4Fe-4S]–dependent dehydration reaction (Fenwick and Ealick 2016). We propose that the chloride ion in the holo-MmLarE crystal structure mimics the hydrogenosulfide ion attached to the cluster that serves as the sulfur donor in the thiolation reaction, as proposed previously for TmLarE (Chatterjee et al. 2022), but also for several tRNA thiolation enzymes (Arragain et al. 2017; Chen et al. 2017; Chen et al. 2020; Shigi et al. 2020; Zhou et al. 2021a; He et al. 2022; Zhou et al. 2022; Bimai et al. 2023) (Figure 7A). The catalytic mechanism would thus involve the formation of an adenylated intermediate followed by a nucleophilic attack of the sulfur atom of the [4Fe-5S]-containing MmLarE on the adenylated intermediate. In the crystal structures of the tRNA thiolation enzymes TtuA and NcsA, a small anionic ligand was also bound to the [4Fe-4S] cluster (Arragain et al. 2017) Furthermore, a [4Fe-5S] catalytic intermediate has previously been trapped in the crystal structure

of thiouracil desulfidase (Zhou et al. 2021b; Zhou et al. 2022), an enzyme that catalyzes a desulfuration reaction, that is, the opposite reaction to that catalyzed by LarE.

Altogether, our structural data are in full agreement with the catalytic assays of [4Fe-4S]-dependent TmLarE (Fellner et al. 2018b; Chatterjee et al. 2022). In these tests, the P2CMN substrate, which is not commercially available and non-trivial to synthesize, came from the incubation mixture of LarB with NaAD and $NaHCO_3$ (Figure 1). Either Liquid Chromatography ESI-MS was used to monitor the disappearance of the substrate and appearance of the monothiolated and bithiolated products, or the formation of the P2TMN product was quantified by measuring the formation of L-lactate by an enzymatic kit after coupling the LarE reaction with the LarC and LarA-catalyzed reactions (Figure 1). These two kinds of activity tests showed that the cluster was essential for the thiolation activity of TmLarE and that a stoichiometric amount of the P2TMN product was formed without adding an exogenous sulfur source, suggesting the presence of a [4Fe-5S] species. This species has likely been formed during assembly of the cluster. Yet, a substantial increase of activity was observed when cysteine together with cysteine desulfurase IscS was used as a sulfur donor (Chatterjee et al. 2022).

3.3 The active site of MmLarE is very similar to that of LpLarE apart from the cluster binding residues

MmLarE exhibited the same fold as LpLarE and a similar active site structure, despite the low sequence identity between the two proteins (26.8 %). Using crystal-based modeling of the main catalytic intermediates of MmLarE and LpLarE, we did not discover major structural differences regarding the protein environment of the reactive centers, namely the [4Fe-4S] cluster and its three cysteines for MmLarE, and the sacrificial cysteine for LpLarE, which are actually found in the same location. In particular, in both enzymes, two conserved residues corresponding to Lys100 and Arg132 in MmLarE, appear to have the same crucial role in catalysis, for bringing together the two substrates and for stabilizing the adenylated intermediates. Moreover, based on the crystal structure of LpLarE and site-directed mutagenesis, it was proposed that Arg181, assisted with Glu200 - with which it forms a bidentate ionic interaction - may abstract the Cα proton of Cys176 (Fellner et al. 2017). However, both Arg181 and Glu200 in LpLarE are fully conserved in both types of LarE proteins (respectively Arg178 and Glu196 in MmLarE) (Figure S1 and S13), which may indicate another function of these residues common to the two proteins.

Finally, given that the sulfuration activity of TmLarE was greatly increased and became catalytic when sulfur was supplied by cysteine and cysteine desulfurase (Chatterjee et al. 2022), the question is raised whether LpLarE could function as a non-sacrificial enzyme and use a different mechanism, when supplied with a sulfur source.

4 Experimental procedures

4.1 Heterologous gene overexpression of MmLarE

The *mmp1239* gene encoding MmLarE from *M. maripaludis* strain S2 (NC_005791.1) was synthesized by Eurofins with codon optimization for expression in *E. coli* and sub-cloned into pET15b (Studier et al. 1990) between the NdeI and BamHI restriction sites to add a 6-histidine tag at the N-terminus, which could be cleaved by the H3C protease. The corresponding protein in UNIPROT (Q6LXV7), which was released later, lacks the nine N-terminal amino acids (MLEVLFQGP).

Competent *E. coli* BL21 (DE3) Star Codon+ cells were transformed with the *larE*-containing plasmid to overexpress MmLarE. A single colony was used to inoculate 200 mL of Luria Broth (LB) medium supplemented with ampicillin (100 $\mu.gmL^{-1}$). 40 mL of this preculture, grown overnight at 37°C, was then used to inoculate 4 L of the same medium. Cells were incubated at 37 °C until the OD_{600} reached 0.6 and protein expression was induced at 16 °C with 0.5 mM isopropyl-γ-D-thiogalactopyranoside (IPTG). Cells were incubated for 18 h at 16°C, collected by centrifugation at 4,000 *g* (4°C) for 15 min, and stored at -80°C until use.

4.2 Aerobic purification of MmLarE

Cells were resuspended in 50 mM Tris-HCl pH 8.5, 500 mM NaCl, 10% glycerol, containing RNase A (2 $\mu g.ml^{-1}$, Fisher), protease inhibitor cocktail (Roche, one tablet per 50 ml), 5 mM β–mercaptoethanol, 1 mM $MgCl_2$, 5 mM imidazole, and disrupted by sonication. Cells debris were removed by centrifugation at 35,000 rpm for one hour at 4°C. The supernatant was then purified using Ni-NTA affinity chromatography (2 x 5 mL HisTrap™ FF columns, Cytiva) in 50 mM Tris-HCl pH 8.5, 300 mM NaCl, 5 mM β–mercaptoethanol and with a linear gradient of 5-500 mM imidazole at 1.5 mL min^{-1} in 100 min. The protein was collected, dialyzed twice against 3 L of 50 mM Tris-HCl pH 7.5, 300 mM NaCl, 5 mM β-mercaptoethanol in the presence of the PreScission Protease (25 µg per mg MmLarE). After concentration with a Vivaspin 20 ultrafiltration membrane (10 kDa cutoff, Sartorius), the protein was further purified at 1 $ml.min^{-1}$ onto a gel filtration column (Hiload 16/60 Superdex 75, Cytiva) equilibrated with 50 mM Tris-HCl pH 8.5, 300 mM NaCl, 5 mM β–mercaptoethanol, using an ÅKTA system. The 'as-purified' protein was concentrated to 5 $mg.ml^{-1}$ with an Amicon Ultra filter device (10 kDa cutoff), frozen in liquid nitrogen and stored at -80°C. The purity of MmLarE was assessed along the purification steps using SDS-PAGE gels and its concentration determined using the Bradford assay (Bradford 1976) (Biorad) using BSA as the standard.

The GST–3C-protease (a gift from S. Mouilleron) was expressed using pGEX-2T recombinant plasmids. After induction at 25°C with 0.1 mM IPTG for 20 h, the protein was purified using glutathione–Sepharose chromatography.

4.3 *In vitro* [Fe-S] cluster reconstitution and purification of holo-MmLarE

The reconstitution of the [4Fe-4S] cluster and purification of holo-MmLarE was performed in a glove box (MBraun) containing less than 0.5 ppm O_2. As-purified MmMarE (100 µM) was first incubated with 10 mM dithiothreitol for 15 min. Then, a 5-fold molar excess of ferrous ammonium sulfate and L-cysteine was added along with *E. coli* cysteine desulfurase CsdA (2 µM). Cluster reconstitution was followed by UV-visible spectroscopy (XL-100 UVICON spectrophotomer equipped with optical fibers) and incubation stopped when $OD_{410}/OD_{280} > 0.3$. After centrifugation for 30 min at 20,000 g, holo-MmLarE was loaded onto a Superdex 200 Increase 10/300 GL gel filtration column (Cytiva) equilibrated in 50 mM Tris-HCl pH 8.5, 150 mM NaCl, 5 mM DTT. The protein was then concentrated to 10 $mg.mL^{-1}$ on a Vivaspin concentrator (10 kDa cutoff, Sartorius), frozen and stored in liquid nitrogen in sealed tubes.

4.4 SEC-MALS analysis

SEC-MALS experiments were performed using an HPLC-MALS system (Shimadzu) equipped with light scattering detector (mini-DAWN TREOS, Wyatt Technology), refractive index detector (Optilab T-rEX, Wyatt Technology) and UV detector (SPD-20A, Shimadzu). Apo- or holo-MmLarE (100 µL at 2 $mg.mL^{-1}$) was injected on a Superdex 200 10/300 GL Increase column (Cytiva) equilibrated in 50 mM Tris-HCl pH 8.5, 300 mM NaCl, 5 mM DTT at a flow rate of 0.5 $mL.min^{-1}$. The molar mass was calculated with the ASTRA 6.1 software (Wyatt Technology) using the Forward Monitor (FM) mode to take into account the fact that the holo-protein absorbs light at the laser wavelength (Velours et al. 2022). A refractive index increment (dn/dc) value of 0.183 $mL.g^{-1}$ was used.

4.5 Mössbauer spectroscopy

The ^{57}Fe metal used for Fe labeling for Mössbauer spectroscopy was rinsed twice with trichloromethane, then solubilized in the glove box with 1.5 molar equivalent H_2SO_4 by heating at 60 °C for 24 hours then 78 °C for 1 hour, under agitation. After centrifugation to remove undissolved particles, the Fe concentration was determined with a calibration curve and the Fish method (Fish 1988). For Mössbauer spectroscopy, as-purified MmLarE was prepared as above, with ferrous ammonium sulfate being replaced by ^{57}Fe during the cluster reconstitution step. Labeled holo-LarE (0.54 mM) in 50 mM Tris-HCl pH 8.5, 180 mM NaCl, 5 mM DTT was frozen in the glove box and stored in liquid nitrogen. Mössbauer spectra were recorded in the constant acceleration mode with a conventional spectrometer (Wissel GmbH) with a multi-channel analyzer (Wissel GmbH) in the time-scale mode . Experiments at 77 K were conducted with an LN_2 bath cryostat (Oxford Instruments). The same type of spectrometer was used in the measurement of high-field, low temperature spectra combined with a helium closed-cycle cryostat equipped with a superconducting magnet (CRYO Industries of America Inc.) operating with the applied field parallel to the γ-rays. Isomer shifts δ are given relative to α-iron at room temperature. After transfer of the data from the multi-channel analyzer to a PC the public domain program Vinda (Gunnlaugsson 2016) running on an Excel 2003 platform was used to analyze the data.

For the simulation of magnetically split spectra the spin Hamiltonian formalism (Gütlich et al. 2011) was utilized. Otherwise, spectra were analyzed by least-squared fits using Lorentzian line shapes.

4.6 Nano LC-MS analysis of as-purified LarE

Protein mass measurements were performed with an electrospray triple time-of-flight (TOF) 4600 mass spectrometer (ABSciex) coupled to an ultra-performance liquid chromatography system (RSLCnano, Thermo Scientific). After loading and desalting the protein sample on a C4 µ-Precolumn reversed-phase (PepMap^{TM} 300 C4, 5 mm length), ESI−MS measurements were conducted in the positive mode, with data being collected for m/z in the range 500−3000. Collision energy was set to 15 eV and nitrogen was used as the collision gas. The Analyst 1.7.1 and Peakview 2.2 softwares were used for acquisition and data processing, respectively. The MaxEnt algorithm was used for mass spectra deconvolution. External calibration was performed using the six-peptide mixture (Sciex).

4.7 Crystallization, X-ray data collection and processing

Crystals of apo-LarE (0.2 x 0.2 x 0.2 mm) were obtained at 18°C in hanging-drops by vapor diffusion by mixing 2 µl of protein at 10 mg ml^{-1} in 50 mM Tris-HCl pH 8.5, 0.15 M NaCl, 5 mM β-mercaptoethanol, and 5 mM AMP-PNP with 2 µl of a 1 ml reservoir solution (1.6 M ammonium sulfate, 2% PEG 400, 0.1 M HEPES pH 7.5, 5 mM AMP-PNP). For cryoprotection, crystals were soaked for a few minutes in the same solution supplemented with 25% glycerol and 5 mM AMP-PNP before flash-freezing in liquid nitrogen. Crystals of holo-MmLarE (0.15 x 0.2 x 0.2 mm) were grown anaerobically at 18°C using the hanging drop method by mixing 2 µL of protein at 3 mg.ml^{-1} in 50 mM Tris-HCl, pH 8.5, 0.15 M NaCl with 1 µL of a reservoir solution containing 4.1 M NaCl, 0.1 M HEPES pH 7.5, and either 0.1 M NaI for Crystal 1 or 10 % glycerol for Crystal 2 (Table 1). For cryoprotection, Crystal 1 was briefly soaked in a solution mixture of paraffine (Hampton research) in a 1:1 ratio. Crystals 1 and 2 were flash-frozen under anaerobic conditions using liquid propane.

Diffraction data were collected on the PROXIMA 1 beamline (Chavas et al. 2021) at the SOLEIL synchrotron (Saint Aubin, France) using an EigerX-16M detector (DECTRIS Ltd)(Table 1). The reflection data of apo-MmLarE and holo-MmLarE (Crystal 2) were indexed and integrated using *XDS*, scaled and merged with *XSCALE,* and the intensities were converted to structure factor amplitudes using *XDSCONV* (Kabsch, 2010). Automatic data indexing by *XDS* revealed that the crystal lattice was primitive hexagonal. The *phenix.xtriage* program (Adams et al. 2010) was used to check for crystal pathologies and detect noncrystallographic symmetry (NCS).

Data collected at the iron edge (7.125 keV), as determined by a fluorescence emission scan, on holo-MmLarE (Crystal 1) were processed with the *autoPROC* pipeline (Vonrhein et al. 2011). The output from *STARANISO* was used since the data showed substantial anisotropy with resolution limits of 3.11 Å / 4.06 Å/ 3.38 Å along the a* / b* / c* reciprocal axes, respectively. Seven heavy atoms were found in the asymmetric unit with *SHELXD* (Sheldrick 2008) (5000 iterations; CFOM 44). These sites were

used as input for *PHASER* in *CCP4* (Winn 2011), followed by 5 cycles of density modification with *PARROT* (Cowtan 2010) using data up to 4 Å resolution. Seven copies of a model, calculated with the recently released *trRosetta* program (Yang et al. 2020), which was in the beta mode at that time, were successfully fitted in the experimental map using *ChimeraX* (Goddard et al. 2018), and refined with *DEN* (Schröder et al. 2010), followed by *phenix.rosetta_refine* (DiMaio et al. 2013), which led to R_{work}/R_{free} of 0.40/0.49, respectively. Since NCS restraints are not applied in *PHENIX.ROSETTA_REFINE*, a model with seven identical chains was then generated, and subjected to *phenix.real_space_refine* using one rigid-body domain per chain for each of the N-terminal (14-178) and C-terminal (194-257) domains, with morphing, secondary structure restraints and NCS constraints. This step improved the map correlation coefficient from 0.509 to 0.587. The resulting model was then used as input for *CRANK2* in MR-SAD mode (Skubák and Pannu 2013), which dramatically improved the model to R_{work} 0.314, with a figure of merit of 0.876. The final model was obtained by alternating manual building in *COOT* (Emsley et al. 2010) and refinement in *autoBUSTER* (Bricogne et al. 2016) using NCS restraints (Smart et al. 2012) and two TLS groups per chain (Schomaker and Trueblood 1968) using the data collected at 12.67 keV on the same crystal.

The structure of apo-MmLarE was solved by molecular replacement using the structure of holo-MmLarE obtained by experimental phasing. Initially, a partial solution containing two N-terminal domains (61% solvent), was obtained using *PHENIX-Phaser* (McCoy et al. 2007). The final molecular replacement solution, which included two full-length polypeptidic chains, was obtained using *SAPTF* (Spherically Averaged Phased Translation Function) in *Molrep* (Vagin and Isupov 2001) by fixing the previously found N-terminal domains and searching for the missing C-terminal domains. The final model was obtained by alternating manual building in *COOT* (Emsley et al. 2010) and refinement in *phenix-refine* (Afonine et al. 2012) using NCS restraints (Headd et al. 2014)and two TLS groups per chain.

4.8 Identification of co-purified compound in as-purified MmLarE and quantification

10 µl hydrochloric acid (300 µM) was added to 90 µl as-purified LarE (300 µM) to precipitate the protein and extract non-covalently bound compounds. After centrifugation at 13,500 rpm for 5 minutes at 4°C, the pH of the supernatant was adjusted to 6.0. The sample was recentrifuged and the supernatant filtered through a 0.22 µm filter (Millipore) prior to analysis. The identification and quantification of co-purified nucleotides were performed using an Agilent 1260 Infinity HPLC system equipped with a quaternary pump, as previously reported (Menegollo et al. 2019). The sample (100 µl) was injected onto a reversed-phase column (Agilent® C18, 2 × 100-mm inner diameter, particle size of 1.8 µm) at 0.5 mL/min and eluted isocratically with 0.1 M ammonium dihydrogen phosphate pH 6.0, 1% methanol. The absorbance at 254 nm was monitored.

4.9 Modeling several catalytic intermediates bound to holo-MmLarE

One carboxylate group was added to the NMN substrate analog bound to LpLarE (PDB code 5UDR, chain A) using *COOT* to model the P2CMN substrate. The superposition of this P2CMN-bound LpLarE model and ATP-bound LpLarE crystal structure (5UDS, chain A) onto holo-MmLarE (chain B) using Secondary-Structure Matching (SSM) in *COOT* (RMSD of 1.80 Å for 223 aligned Cαs and 1.804 Å for 223 aligned Cαs, respectively) gave the positions of P2CMN and ATP, relative to MmLarE, respectively. Maintaining the adenine ring of AMP and the phosphate group of PC2MN in place, a manual translation of ~1.7 Å of P2CMN in *COOT* was sufficient to bring it sufficiently close to ATP to make a covalent link between the oxygen atom of the carboxylate group of the substrate and the α phosphorus atom of ATP to give the adenylated intermediate I. The [4Fe-5S] cluster in holo-MmLarE was modeled by replacing the bound chloride atom by a hydrogenosulfide ion. Adenylated intermediates I and II were generated using Lidia (Emsley 2017), the ligand builder program in *COOT*, based on the following SMILES ID (Nc1ncnc2c1ncn2[C@@H]1OC@H[C@H]1O).

Likewise, the models of the LpLarE catalytic intermediates were based on chain A of NMN-bound LpLarE (PDB code 5UDR). PC2MN was built from NMN in *COOT,* and ATP was positioned from ATP-bound LpLarE (PDB code 5UDS, chain A; RMSD of 0.52Å for 256 aligned Cαs). Additional modifications of the model included the incorporation of 18 residues corresponding to the 127-145 loop, which were not observed in NMN-bound LarE, from AMP-bound LpLarE (PDB code 5UDT, chain A), as well as the modeling of the side chain of Asp128 based on the AlphaFold prediction (ID: AF-F9UST4-F1) and that of Lys101 based on ATP-bound LpLarE (PDB code 5UDS, chain C). An alternative conformation of Trp97 was also introduced, corresponding to a distinct conformation observed in chain B of the 5UDR structure.

All models were built by alternating manual positioning of the substrates in *COOT* and minimizing the energy of the model using the Geometry-Minimization program in *PHENIX* (Afonine et al. 2012). The interactions were then analyzed using *LIGPLOT* (Laskowski and Swindells 2011). The models are accessible at the following link https://www.doi.org : LpLarE initial state 10.13140/RG.2.2.25986.45764 ; LpLarE adenylated intermediate 1 10.13140/RG.2.2.30705.04962 ; LpLarE adenylated intermediate 2 10.13140/RG.2.2.27349.60645 ; LpLarE final state 10.13140/RG.2.2.20638.72008 ; MmLarE initial state 10.13140/RG.2.2.22316.44167 ; MmLarE adenylated intermediate 1 10.13140/RG.2.2.24833.02400 ; MmLarE adenylated intermediate 2 10.13140/RG.2.2.27349.60645 ; MmLarE final state 10.13140/RG.2.2.11411.25128.

Accession numbers

PDB codes : 8CNZ, holo-MmLarE used for SAD phasing; 8CP4, holo-MmLarE refined at 3.2 Å resolution ; 8CP3, apo-MmLarE.

Supplementary material description

Acknowledgements

We thank SOLEIL for provision of synchrotron radiation facilities (proposal 20191181), Pierre Legrand for assistance in using beamline PROXIMA 1, and Laïla Sago for performing nano LC-MS analysis. This work was supported by the French State Program 'Investissements d'Avenir' (Grants "LABEX DYNAMO", ANR-11-LABX-0011) and has benefited from the facilities and expertise of the Macromolecular Interaction Platform of I2BC.

References

Adams, P.D., Afonine, P.V., Bunkoczi, G., Chen, V.B., Davis, I.W., Echols, N., Headd, J.J., Hung, L.W., Kapral, G.J., Grosse-Kunstleve, R.W. et al. 2010. PHENIX: a comprehensive Python-based system for macromolecular structure solution. *Acta Crystallogr D Biol Crystallogr* **66**(Pt 2): 213-221.

Afonine, P.V., Grosse-Kunstleve, R.W., Echols, N., Headd, J.J., Moriarty, N.W., Mustyakimov, M., Terwilliger, T.C., Urzhumtsev, A., Zwart, P.H., and Adams, P.D. 2012. Towards automated crystallographic structure refinement with phenix.refine. *Acta Crystallogr D Biol Crystallogr* **68**: 352-367.

Arndt, U.W., Crowther, R.A., and Mallett, J.F. 1968. A computer-linked cathode-ray tube microdensitometer for x-ray crystallography. *J Sci Instrum* **1**(5): 510-516.

Arragain, S., Bimai, O., Legrand, P., Caillat, S., Ravanat, J.L., Touati, N., Binet, L., Atta, M., Fontecave, M., and Golinelli-Pimpaneau, B. 2017. Nonredox thiolation in tRNA

occurring via sulfur activation by a [4Fe-4S] cluster. *Proc Natl Acad Sci U S A* **114**(28): 7355-7360.
Beinert, H., Holm, R.H., and Münck, E. 1997. Iron-Sulfur Clusters: Nature's Modular, Multipurpose Structures. *Science* **277**(5326): 653-659.
Bimai, O., Arragain, S., and Golinelli-Pimpaneau, B. 2020. Structure-based mechanistic insights into catalysis by tRNA thiolation enzymes. *Curr Opin Struct Biol* **65**: 69-78.
Bimai, O., Legrand, P., Ravanat, J.L., Touati, N., Zhou, J., He, N., Lénon, M., Barras, F., Fontecave, M., and Golinelli-Pimpaneau, B. 2023. The thiolation of uridine 34 in tRNA, which contols protein translation, depends on a [4Fe-4S]-cluster in *Methanococcus maripaludis*. *Sci Rep* **13**: 5351.
Bogdan, J.A., Nazariolarrieu, J., Sarwar, J., Alexander, P., and Blake, M.S. 2001. *Bordetella pertussis* autoregulates pertussis toxin production through the metabolism of cysteine. *Infect Immun* **69**: 6823.
Bouvier, D., Labessan, N., Clemancey, M., Latour, J.M., Ravanat, J.L., Fontecave, M., and Atta, M. 2014. TtcA a new tRNA-thioltransferase with an Fe-S cluster. *Nucleic Acids Res* **42**(12): 7960-7970.
Bradford, M.M. 1976. A rapid and sensitive method for the quantitation of microgram quantities of protein utilizing the principle of protein-dye binding. *Anal Biochem* **72**: 248-254.
Bricogne, G., Blanc, E., Brandl, M., Flensburg, C., Keller, P., Paciorek, W., Roversi, P., Sharff, A., Smart, O.S., Vonrhein, C. et al. 2016. *BUSTER version 2102 Cambridge, United Kingdom: Global Phasing Ltd*.
Brünger, A.T. 1992. Free R value: a novel statistical quantity for assessing the accuracy of crystal structures. *Nature* **355**(6359): 472-475.
Bunkóczi, G. and Read, R.J. 2011. Improvement of molecular-replacement models with Sculptor. *Acta Crystallogr D Biol Crystallogr* **67**(4): 303-312.
Chatterjee, S. and Hausinger, R.P. 2022. Sulfur incorporation into biomolecules: recent advances. *Crit Rev Biochem Mol Biol* **57**(5-6): 461-476.
Chatterjee, S., Parson, K.F., Ruotolo, B.T., McCracken, J., Hu, J., and Hausinger, R.P. 2022. Characterization of a [4Fe-4S]-dependent LarE sulfur insertase that facilitates nickel-pincer nucleotide cofactor biosynthesis in *Thermotoga maritima*. *J Biol Chem* **298**(7): 102131.
Chavas, L.M.G., Gourhant, P., Guimaraes, B.G., Isabet, T., Legrand, P., Lener, R., Montaville, P., S., S., and A., T. 2021. PROXIMA-1 beamline for macromolecular crystallography measurements at Synchrotron SOLEIL. *J Synchrotron Rad* **28**: 970-976.
Chen, M., Asai, S.I., Narai, S., Nambu, S., Omura, N., Sakaguchi, Y., Suzuki, T., Ikeda-Saito, M., Watanabe, K., Yao, M. et al. 2017. Biochemical and structural characterization of oxygen-sensitive 2-thiouridine synthesis catalyzed by an iron-sulfur protein TtuA. *Proc Natl Acad Sci U S A* **114**(19): 4954-4959.
Chen, M., Ishizaka, M., Narai, S., Horitani, M., Shigi, N., Yao, M., and Tanaka, Y. 2020. The [4Fe-4S] cluster of sulfurtransferase TtuA desulfurizes TtuB during tRNA modification in *Thermus thermophilus*. *Commun Biol* **3**(1): 168.
Cicchillo, R.M., Iwig, D.F., Jones, A.D., Nesbitt, N.M., Baleanu-Gogonea, C., Souder, M.G., Tu, L., and Booker, S.J. 2004. Lipoyl synthase requires two equivalents of S-adenosyl-L-methionine to synthesize one equivalent of lipoic acid. *Biochemistry* **43**(21): 6378-6386.
Cowtan, K. 2010. Recent developments in classical density modification. *Acta Crystallogr D Biol Crystallogr* **66**: 470-478.

Desguin, B., Goffin, P., Viaene, E., Kleerebezem, M., Martin-Diaconescu, V., Maroney, M.J., Declercq, J.P., Soumillion, P., and Hols, P. 2014. Lactate racemase is a nickel-dependent enzyme activated by a widespread maturation system. *Nat Commun* **5**: 3615.

Diederichs, K. and Karplus, P.A. 1997. Improved R-factors for diffraction data analysis in macromolecular crystallography. *Nat Struct Biol* **4**(4): 269-275.

-. 2013. Better models by discarding data? *Acta Crystallogr D Biol Crystallogr* **69**(7): 1215-1222.

DiMaio, F., Echols, N., Headd, J.J., Terwilliger, T.C., Adams, P.D., and David Baker, D. 2013. Improved low-resolution crystallographic refinement with Phenix and Rosetta. *Nat Methods* **10**(11): 1102–1104.

Emsley, P. 2017. Tools for ligand validation in COOT. *Acta Crystallogr D Biol Crystallogr* **73**: 203-2010.

Emsley, P., Lohkamp, B., Scott, W.G., and Cowtan, K. 2010. Features and development of Coot. *Acta Crystallogr D Biol Crystallogr* **66**(Pt 4): 486-501.

Fellner, M., Desguin, B., Hausinger, R.P., and Hu, J. 2017. Structural insights into the catalytic mechanism of a sacrificial sulfur insertase of the N-type ATP pyrophosphatase family, LarE. *Proc Natl Acad Sci U S A* **114**(34): 9074-9079.

Fellner, M., Hausinger, R.P., and Hu, J. 2018a. A structural perspective on the PP-loop ATP pyrophosphatase family. *Crit Rev Biochem Mol Biol* **53**(6): 607-622.

Fellner, M., Rankin, J.A., Desguin, B., Hu, J., and Hausinger, R.P. 2018b. Analysis of the Active Site Cysteine Residue of the Sacrificial Sulfur Insertase LarE from *Lactobacillus plantarum*. *Biochemistry* **57**(38): 5513-5523

Fenwick, M.K. and Ealick, S.E. 2016. Crystal structures of the iron-sulfur cluster dependent quinolinate synthase in complex with dihydroxyacetone phosphate, iminoaspartate analogs, and quinolinate. *Biochemistry* **55**(30): 4135–4139.

Fish, W.W. 1988. Rapid Colorimetric Micromethod for the Quantitation of Complexed Iron in Biological Samples. *Methods in Enzymology* **158**: 357-364.

Fontecave, M., Ollagnier-de-Choudens, S., and Mulliez, E. 2003. Biological radical sulfur insertion reactions. *Chem Rev* **103**(6): 2149-2166.

Forouhar, F., Arragain, S., Atta, M., Gambarelli, S., Mouesca, J.M., Hussain, M., Xiao, R., Kieffer-Jaquinod, S., Seetharaman, J., Acton, T.B. et al. 2013. Two Fe-S clusters catalyze sulfur insertion by radical-SAM methylthiotransferases. *Nat Chem Biol* **9**(5): 333-338.

Fugate, C.J. and Jarrett, J.T. 2012. Biotin synthase: insights into radical-mediated carbon-sulfur bond formation. *Biochim Biophys Acta* **1824**(11): 1213-1222.

Gabler, F., Nam, S.Z., Till, S., Mirdita, M., Steinegger, M., Söding, J., Lupas, A.N., and Alva, V. 2020. Protein Sequence Analysis Using the MPI Bioinformatics Toolkit. *Curr Protoc Bioinformatics* **72**(1): e108.

Goddard, T.D., Huang, C.C., Meng, E.C., Pettersen, E.F., Couch, G.S., Morris, J.H., and Ferrin, T.E. 2018. UCSF ChimeraX: Meeting modern challenges in visualization and analysis. *Protein Sci* **27**(1): 14-25.

Goffin, P., Deghorain, M., Mainardi, J.L., Tytgat, I., Champomier-Vergès, M.C., Kleerebezem, M., and Hols, P. 2005. Lactate Racemization as a Rescue Pathway for Supplying D-Lactate to the Cell Wall Biosynthesis Machinery in *Lactobacillus plantarum*. *J Bacteriol* **187**(19): 6750–6761.

Golinelli-Pimpaneau, B. 2022. Prediction of the Iron–Sulfur Binding Sites in Proteins Using the Highly Accurate Three-Dimensional Models Calculated by AlphaFold and RoseTTAFold. *Inorganics* **10**(1): 2.

Gouet, P., Courcelle, E., Stuart, D.I., and Metoz, F. 1999. ESPript: analysis of multiple sequence alignments in PostScript. *Bioinformatics* **15**(4): 305-308.
Gunnlaugsson, H.P. 2016. Spreadsheet based analysis of Mössbauer spectra. *Hyperfine Interact* **237**(1): 13-18.
Gütlich, P., Bill, E., and Trautwein, A.X. 2011. *Mössbauer Spectroscopy and Transition Metal Chemistry*. Springer Berlin Heidelberg, Berlin, Heidelberg.
He, N., Zhou, J., Bimai, O., Oltmanns, J., Ravanat, J.L., Velours, C., Schünemann, V., Fontecave, M., and Golinelli-Pimpaneau, B. 2022. A subclass of archaeal U8-tRNA sulfurases requires a [4Fe-4S] cluster for catalysis. *Nucleic Acids Res* **50**(4): 12969-12978.
Headd, J.J., Echols, N., Afonine, P.V., Moriarty, N.W., Gildea, R.J., and Adams, P.D. 2014. Flexible torsion-angle noncrystallographic symmetry restraints for improved macromolecular structure refinement. *Acta Crystallogr D Biol Crystallogr* **70**(5): 1346-1356.
Jumper, J., Evans, R., Pritzel, A., Green, T., Figurnov, M., Ronneberger, O., Tunyasuvunakool, K., Bates, R., Žídek, A., Potapenko, A. et al. 2021. Highly accurate protein structure prediction with AlphaFold. *Nature* **596**(7873): 583-589.
Kabsch, W. 2010. XDS. *Acta Crystallogr D Biol Crystallogr.* **66***():125-32.*
Krissinel, E. 2010. Crystal contacts as nature's docking solutions. *J Comput Chem* **31**(1): 133-143.
Laskowski, R.A. and Swindells, M.B. 2011. LigPlot+: multiple ligand-protein interaction diagrams for drug discovery. *J Chem Inf* **51**(10): 2778-2786.
McCoy, A.J., Grosse-Kunstleve, R.W., Adams, P.D., Winn, M.D., Storoni, L.C., and Read, R.J. 2007. Phaser crystallographic software. *Journal of Applied Crystallography* **40**: 658-674.
Menegollo, M., Tessari, I., Bubacco, L., and Szabadkai, G. 2019. Determination of ATP, ADP, and AMP Levels by Reversed-Phase High-Performance Liquid Chromatography in Cultured Cells. In *Methods in molecular biology*, Vol 1925, pp. 223-232. Clifton, N.J.
Mueller, E.G., Palenchar, P.M., and Buck, C.J. 2001. The role of the cysteine residues of ThiI in the generation of 4-thiouridine in tRNA. *J Biol Chem* **276**(36): 33588-33595.
Pandelia, M.E., Lanz, N.D., Booker, S.J., and Krebs, C. 2015. Mössbauer spectroscopy of Fe/S proteins. *Biochim Biophys Acta* **1853**(6): 1395-1405.
Schomaker, V. and Trueblood, K.N. 1968. On the Rigid-Body Motion of Molecules in Crystals. *Acta Cryst B* **24**: 63.
Schröder, G.F., Michael Levitt, M., and Axel T Brunger, A.T. 2010. Super-resolution biomolecular crystallography with low-resolution data. *Nature* **464**(7292): 1218-1222.
Schünemann, V. 2021. From Small Molecules to Complex Systems: A Survey of Chemical and Biological Applications of the Mössbauer Effect. In *Modern Mössbauer Spectroscopy Topics in Applied Physics*, Vol 137 (ed. Y. Yoshida and G. Langouche). Springer Singapore.
Schünemann, V., Meier, C.B., Meyer-klaucke, W., Winkler, H., Trautwein, A.X., Knappskog, P.M., Toska, K., and Haavik, J. 1999. Iron coordination geometry in full-length, truncated, and dehydrated forms of human tyrosine hydroxylase studied by Mössbauer and X-ray absorption spectroscopy. *J Biol Inorg Chem* **4**: 223-231.
Sheldrick, G.M. 2008. A short history of SHELX. *Acta Crystallogr A* **64**(1): 112-122.
Shigi, N. 2018. Recent Advances in Our Understanding of the Biosynthesis of Sulfur Modifications in tRNAs. *Front Microbiol* **9**: 2679.
-. 2021. Biosynthesis and Degradation of Sulfur Modifications in tRNAs. *Int J Mol Sci* **22**(21): 11937.

Shigi, N., Horitani, M., Miyauchi, K., Suzuki, T., and Kuroki, M. 2020. An ancient type of MnmA protein is an iron-sulfur cluster-dependent sulfurtransferase for tRNA anticodons. *RNA* **26**(3): 240-250.

Sievers, F., Wilm, A., Dineen, D., Gibson, T.J., Karplus, K., Li, W., Lopez, R., McWilliam, H., Remmert, M., Soding, J. et al. 2011. Fast, scalable generation of high-quality protein multiple sequence alignments using Clustal Omega. *Mol Syst Biol* **7**: 539.

Skubák, P. and Pannu, N.S. 2013. Automatic protein structure solution from weak X-ray data *Nat Commun* **4**: 2777.

Smart, O.S., Womack, T.O., Flensburg, C., Keller, P., Paciorek, W., Sharff, A., Vonrhein, C., and Bricogne, G. 2012. Exploiting structure similarity in refinement: automated NCS and target-structure restraints in BUSTER. *Acta Crystallogr D Biol Crystallogr* **68**(4): 368-380.

Studier, F.W., Rosenberg, A.H., Dunn, J.J., and Dubendorff, J.W. 1990. Use of T7 RNA polymerase to direct expression of cloned genes. *Methods Enzymol* **185**: 60-89.

Tickle, I.J., R.A., L., and Moss, D.S. 1998. Rfree and the Rfree ratio. Part I: derivation of expected values of cross-validation residuals used in macromolecular least-squares refinement. *Acta Crystallographica D* **54**: 547-557.

Ueda, C., Langton, M., and Pandelia, M.E. 2021. Characterization of Fe-S Clusters in Proteins by Mössbauer Spectroscopy. *Methods Mol Biol* **2353**: 281-305.

Vagin, A.A. and Isupov, M.N. 2001. Spherically averaged phased translation function and its application to the search for molecules and fragments in electron-density maps. *Acta Crystallogr D Biol Crystallogr* **57**(10): 1451-1456.

Velours, C., Zhou, J., Zecchin, P., He, N., Salameh, M., Golinelli-Cohen, M.P., and Golinelli-Pimpaneau, B. 2022. Determination of the Absolute Molar Mass of [Fe-S]-Containing Proteins Using Size Exclusion Chromatography-Multi-Angle Light Scattering (SEC-MALS). *Biomolecules* **12**(2): 270.

Vonrhein, C., Flensburg, C., Keller, P., Sharff, A., Smart, O., Paciorek, W., Womack, T., and Bricogne, G. 2011. Data processing and analysis with the autoPROC toolbox. *Acta Crystallogr D Biol Crystallogr* **67**(Pt 4): 293-302.

Winn, M.D. 2011. Overview of the CCP4 suite and current developments. *Acta Crystallogr D Biol Crystallogr* **67**: 235-242.

Yang, J., Anishchenko, I., Park, H., Peng, Z., Ovchinnikov, S., and Baker, D. 2020. Improved protein structure prediction using predicted interresidue orientations. *Proc Natl Acad Sci U S A* **117**(3): 1496-1503.

Yariv, B., Yariv, E., Kessel, A., Masrati, G., Chorin, A.B., Martz, E., Mayrose, I., Pupko, T., and Ben-Tal, N. 2023. Using evolutionary data to make sense of macromolecules with a 'face-lifted' ConSurf. *Protein Science* **32**(3): e4582.

Zhou, J., Bimai, O., Arragain, S., Pecqueur, L., and Golinelli-Pimpaneau, B. 2022. TtuA and TudS, two [4Fe-4S]-dependent enzymes catalyzing non-redox sulfuration or desulfuration reactions. In *Encyclopedia of Inorganic and Bioinorganic Chemistry*, (ed. S.E. Wiley), pp. 1-16. Wiley, Chichester, UK.

Zhou, J., Lénon, M., Touati, N., Ravanat, J.-L., Velours, C., Fontecave, M., Barras, F., and Golinelli-Pimpaneau, B. 2021a. Iron sulfur biology invades tRNA modification: the case of U34 sulfuration. *Nucleic Acids Res* **49**: 3997-4007.

Zhou, J., Pecqueur, L., Aučynaitė, A., Fuchs, J., Rutkienė, R., Vaitekūnas, J., Meškys, R., Boll, M., Fontecave, M., Urbonavičius, J. et al. 2021b. Structural evidence for a [4Fe-5S] intermediate in the non-redox desulfuration of thiouracil. *Angew Chem Int Ed Engl* **60**: 424-431.

Table 1: Data collection and refinement statistics

	holo-MmLarE (Crystal 1)		holo-MmLarE (Crystal 2)	apo-MmLarE
PDB code	8CNZ		8CP4	8CP3
Data collection				
Photon energy (keV)	7.125	12.670	12.670	12.670
Space group	C 2 2 2_1		C 2 2 2_1	R 3 2 :H
Cell dimensions				
a, *b*, *c* (Å)	187.4 209.6 195.7	187.5 209.2 195.8	186.2 212.7 196.7	144.8 144.8 193.6
α, β, γ (°)	90 90 90	90 90 90	90 90 90	90 90 120
Resolution (Å)	139.7 – 3.16 (3.45 – 3.16)	113.7 – 3.14 (3.48 – 3.14)	46.78 – 3.19 (3.39 – 3.19)	48.18 – 2.35 (2.49 – 2.35)
R_{sym} or R_{merge}[1]	0.35 (2.64)	0.170 (1.17)	0.152 (2.34)	0.065 (2.37)
R_{meas}[2]	0.36 (2.70)	0.186 (1.27)	0.163 (2.10)	0.067 (2.43)
$I / \sigma I$	7.5 (1.7)	7.0 (1.7)	7.6 (0.77)	25.4 (0.95)
Completeness (%)				
spherical	70.0 (15.1)	65.7 (12.6)	99.7 (98.2)	99.7 (98.5)
ellipsoidal	93.7 (59.6)	93.7 (65.8)	-	-
No. unique reflections	867284	263306 (14083)	64718 (6222)	32562 (5128)
Redundancy	18.7 (20.6)	6.0 (6.4)	7.8 (7.8)	20.7 (19.1)
CC(1/2)[3]	0.99 (0.64)	1.00 (0.61)	1.00 (0.35)	1.00 (0.501)
Refinement				
Resolution (Å)		55.37 – 3.60	47.87 – 3.19	45.16 – 2.35
No. reflections		40205	64593	32558
R_{work} / R_{free}[4]		0.253 / 0.280	0.216 / 0.252	0.231 / 0.250
No. atoms				
Protein		14378	14441	3716
[4Fe-4S]		56	56	-
AMP		-	23	-
AMP-PNP		-	-	88
Cl		5	11	-
I		4	-	-
SO_4		-	-	24
Glycerol		-	-	6
β-mercaptoethanol		-	-	8
Water		-	4	30
B-factors				
Macromolecule		118.4	114.4	102.7
[4Fe-4S]		84.8	104.5	-
AMP		-	129.3	-
AMP-PNP		-	-	78.0
Cl		82.3	133.2	-
I		90.3	-	-
SO_4		-	-	121.5
Glycerol		-	-	87.3
β-mercaptoethanol		-	-	102.6
Water		-	108.1	83.4
R.m.s. deviations				
Bond lengths (Å)		0.007	0.014	0.008
Bond angles (°)		0.92	1.47	1.095
Ramachandran				
Favored (%)		94.5	95.9	98.3
Allowed (%)		4.5	3.8	1.7
Outliers (%)		1.0	0.3	0.0
Molprobity Clashscore		5.6	13.7	5.5

[1] (Arndt et al. 1968)
[2] (Diederichs and Karplus 1997)
[3] (Diederichs and Karplus 2013)
[4] (Brünger 1992; Tickle et al. 1998)

Figure legends

Figure 1: Biosynthesis of the nickel-pincer nucleotide (NPN) cofactor of lactate racemase. The biosynthesis of the LarA cofactor, NPN, involves three enzymes: LarB, LarE and LarC. LarB is a carboxylase/hydrolase of nicotinic acid adenine dinucleotide (NaAD), which forms P2CMN (pyrimidinium-3,5-biscarboxylic acid mononucleotide). LarE catalyzes the ATP-dependent sulfur insertion into the two carboxylate groups of P2CMN to form P2TMN (pyridinium-3,5-bisthiocarboxylic acid mononucleotide). LarC is a CTP-dependent enzyme that inserts nickel in to P2TMN to form NPN.

Figure 2. **Spectroscopic characterization of MmLarE. A** UV-visible spectrum of 30 µM as-purified MmLarE (dotted line) and holo-MmLarE (solid line) in 50 mM Tris-HCl, pH 8.5, 300 mM NaCl, and 5 mM 2-β-mercaptoethanol. **B** Mössbauer spectrum at 77 K and B_{ext}=0 T of holo-MmLarE (540 µM) in 50 mM TRIS-HCl pH 8.5, 180 mM NaCl, 5 mM DTT, after reconstitution of the cluster with ^{57}Fe. The red solid line is a simulation with two components (1 and 2) and the parameters given in Table S1.

Figure 3. **Determination of the crystal structure of holo-MmLarE by SAD phasing. A** Organization of the 7 molecules in the asymmetric unit of holo-MmLarE. The experimental anomalous map contoured at 5 σ is shown in grey, with the position of the seven super-heavy atoms in the asymmetric unit in stick representation. **B** Dimer of holo-MmLarE. Each monomer is colored in orange and green, with the N-terminal and C-terminal domains shown in dark and light colors, respectively. The [4Fe-4S] cluster is shown is stick representation. **C** Superposition of the Cα trace of the seven monomers of the holo-MmLarE structure solved by SAD. The colors of the monomers are limon (A), tv_red (B), limegreen (C), cyan (D), orange (E), white (F), skyblue (G). **D** Stereoview of the C-terminal dimerization region of MmLarE. Electrostatic interactions (between Asp254 and Lys250, between Lys224 and Glu237 and between Lys258 and Glu221 from both chains) and H-bonds less than 3.2 Å are indicated as dashed lines.

Figure 4. **Active site structure of holo-MmLarE**. **A** The [4Fe-4S] cluster is bound to the three conserved cysteines. An anomalous electron density map at the Fe edge, contoured at 2 σ and shown in green, is superimposed onto the active site of molecule A of holo-MmLarE. **B** In molecule A, the fourth, non-protein bonded Fe atom lies 2.1Å and 2.2 Å away from two oxygens of the phosphate group of AMP. An electron density map, omitting AMP and contoured at 2.5 σ, is shown in magenta. **C** In the other molecules in the asymmetric unit, an extra electron density near the fourth, non-protein bonded Fe atom, was attributed to a chloride ion, located 2.2 Å away from that Fe atom. The electron density map, omitting Cl^- and contoured at 2.5 σ, is shown in magenta.

Figure 5: The apo-MmLarE structure. A Superposition of the N-terminal domains of molecules A of apo-MmLarE and holo-MmLarE with LSQ in COOT (RMSD of 1.56 Å over 156 Cα atoms). The C-terminal domains display a rotation angle of 125° and translation of 17 Å. **B** Superposition of the N-terminal domains of molecule B of apo-MmLarE and of one monomer of holo-MmLarE (RMSD of 1.37 Å over 156 Cα atoms). The C-terminal domains display a rotation angle of 167° and translation of 27 Å. **C** Comparison of the dimers of holo-LarE (monomers in orange and green) and apo-LarE (monomers in violet and pink). **D** Zoom of the disulfide bond between CysA96 (molecule A) and CysB174 (molecule B), which links the two molecules in the asymmetric unit in apo-MmLarE. An electron density map omitting the two cysteines and contoured at 2 σ was superimposed onto the structure. **E** AMP-PNP is present in the active site of apo-MmLarE. The γ-phosphate displays two alternative conformations. An electron density map, omitting AMP-PNP and contoured at 2.5 σ, is shown in magenta.

Figure 6: Comparison of the crystal structures of holo-MmLarE and LpLarE monomers. **A** Superposition of the N-terminal domains of molecule A of holo-MmLarE (in orange) in complex with AMP, and LpLarE (in blue) in complex with NMN (PDB code 5UDR, mol A) in *PYMOL*. The RMSD was 1.2 Å over 616 Cαs. The C-terminal domains of holo-MmLarE and LpLarE are shown in tan and cyan, respectively, with the linkers in yellow (MmLarE) and green (LpLarE). NMN (from the LpLarE crystal) and AMP (from the MmLarE crystal) are shown as sticks, in the same color as the domain to which they belong. The cluster of holo-MmLarE is shown in stick representation. **B** Zoom of the superposed active sites of holo-MmLarE and LpLarE. **C** Electrostatic surface of holo-MmLarE in complex with AMP (left) and LpLarE in complex with ATP and Mg^{2+} (green sphere) (PDB code 5UDS, middle) or NMN (PDB code 5UDR, right), calculated with *APBS* and colored by the electrostatic

potential from red (negative charge) to blue (positive charge). The ligands and cluster are shown in stick representation. **D** Zoom of the active sites of the structures shown in (A) colored by residue conservation using *CONSURF* (Yariv et al. 2023).

Figure 7: Catalytic mechanism and model of substrate analogue NMN bound to holo-MmLarE. **A** Proposed catalytic mechanism of ATP-dependent [4Fe-4S]-containing LarE enzymes, in which the sulfur atom attached to a [4Fe-5S] cluster intermediate is used as a sulfur donor for the thiolation reaction. This mechanism involves the formation of a P2CMN adenylate intermediate I and a tetrahedral hydrogenosulfoadenylate intermediate II. **B** Superposition of the crystal structures of holo-MmLarE (molecule B, in orange), apo-MmLarE in complex with AMP-PNP (in magenta) and LpLarE in complex with NMN (PDB code 5UDR, in blue) or ATP (PDB code 5UDS, in cyan). In this model of NMN bound to holo-MmLarE, the chloride atom attached to the cluster (shown as a magenta sphere), which mimics the sulfur atom used as the sulfur donor for the thiolation reaction, is located 5.4 Å away from the C4 carbon atom of the nicotinamide ring of NMN, which becomes adenylated.

Figure 1: Biosynthesis of the nickel-pincer nucleotide (NPN) cofactor of lactate racemase. The biosynthesis of the LarA cofactor, NPN, involves three enzymes: LarB, LarE and LarC. LarB is a carboxylase/hydrolase of nicotinic acid adenine dinucleotide (NaAD), which forms P2CMN (pyrimidinium-3,5-biscarboxylic acid mononucleotide). LarE catalyzes the ATP-dependent sulfur insertion into the two carboxylate groups of P2CMN to form P2TMN (pyridinium-3,5-bisthiocarboxylic acid mononucleotide). LarC is a CTP-dependent enzyme that inserts nickel in to P2TMN to form NPN.

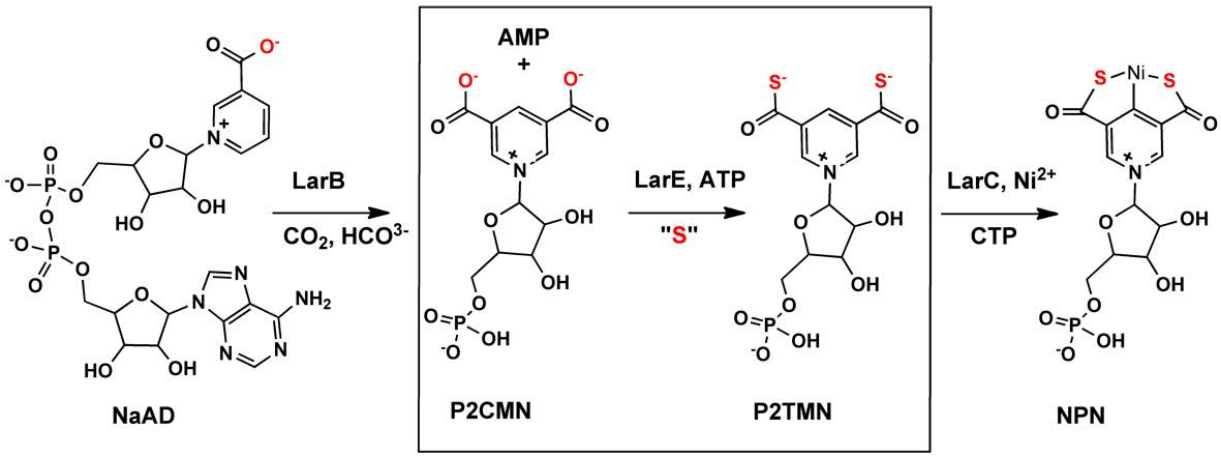

Figure 2. **Spectroscopic characterization of MmLarE. A** UV-visible spectrum of 30 µM as-purified MmLarE (dotted line) and holo-MmLarE (solid line) in 50 mM Tris-HCl, pH 8.5, 300 mM NaCl, and 5 mM 2-β-mercaptoethanol. **B** Mössbauer spectrum at 77 K and B_{ext}=0 T of holo-MmLarE (540 µM) in 50 mM TRIS-HCl pH 8.5, 180 mM NaCl, 5 mM DTT, after reconstitution of the cluster with ^{57}Fe. The red solid line is a simulation with two components (1 and 2) and the parameters given in Table S1.

A

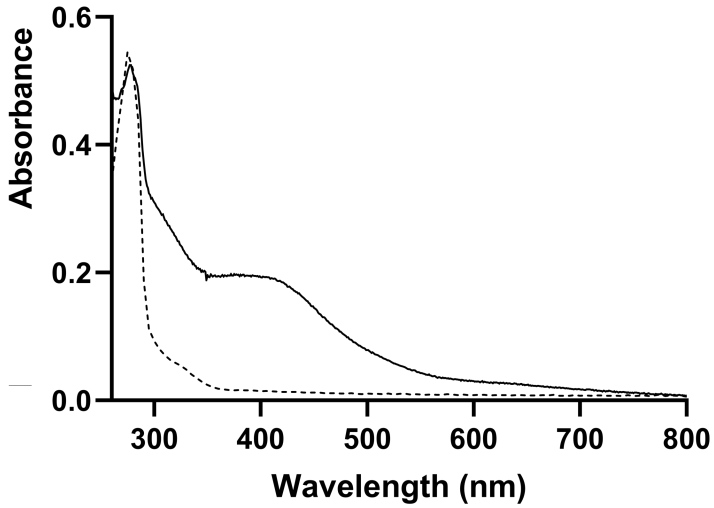

B

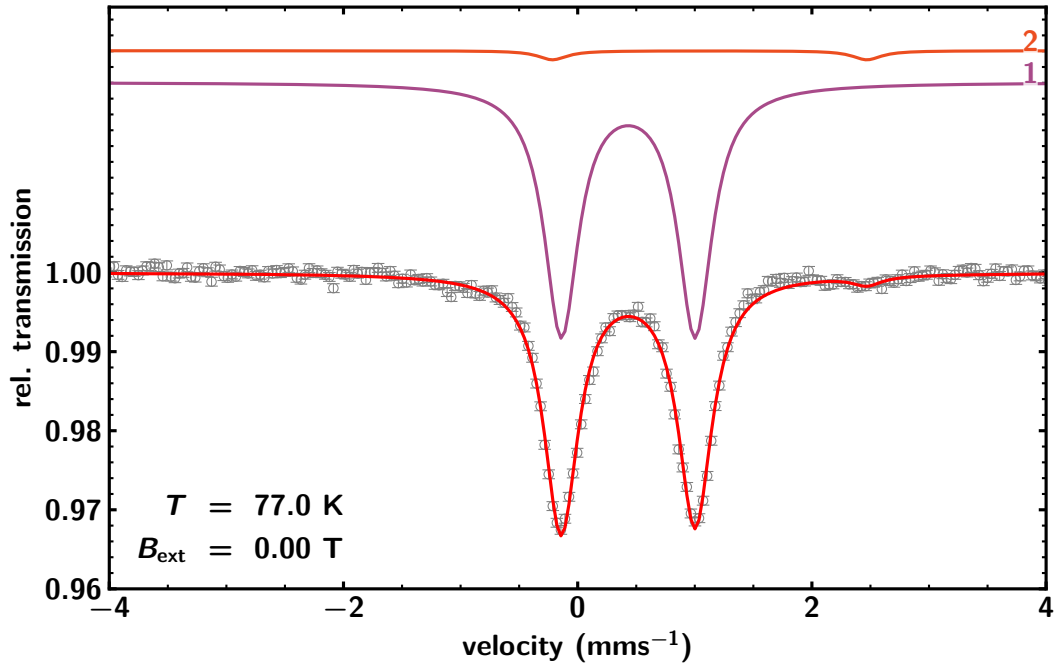

Figure 3. **Determination of the crystal structure of holo-MmLarE by SAD phasing. A** Organization of the 7 molecules in the asymmetric unit of holo-MmLarE. The experimental anomalous map contoured at 5 σ is shown in grey, with the position of the seven super-heavy atoms in the asymmetric unit in stick representation. **B** Dimer of holo-MmLarE. Each monomer is colored in orange and green, with the N-terminal and C-terminal domains shown in dark and light colors, respectively. The [4Fe-4S] cluster is shown is stick representation. **C** Superposition of the Cα trace of the seven monomers of the holo-MmLarE structure solved by SAD. The colors of the monomers are limon (A), tv_red (B), limegreen (C), cyan (D), orange (E), white (F), skyblue (G). **D** Stereoview of the C-terminal dimerization region of MmLarE. Electrostatic interactions (between Asp254 and Lys250, between Lys224 and Glu237 and between Lys258 and Glu221 from both chains) and H-bonds less than 3.2 Å are indicated as dashed lines.

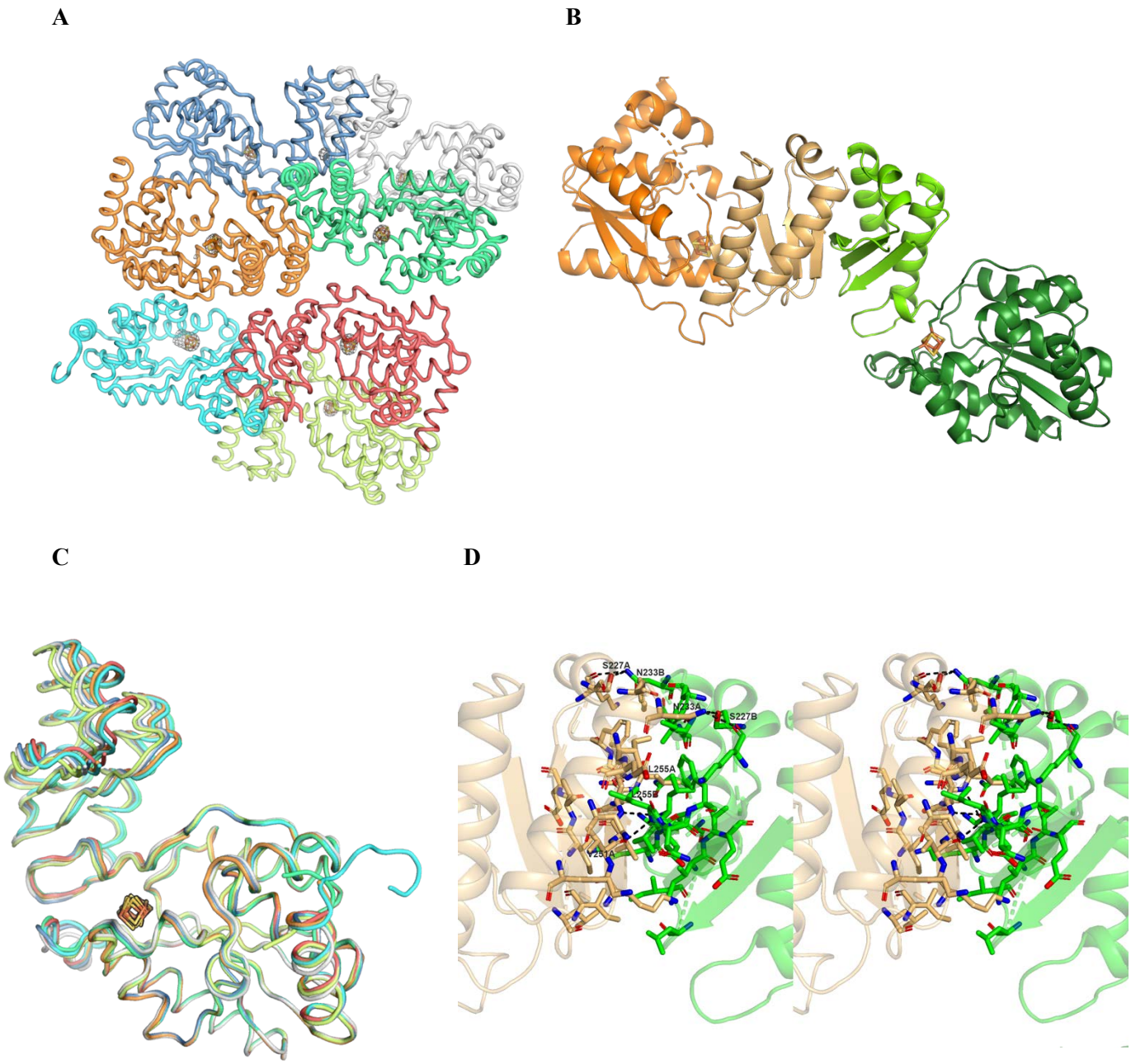

Figure 4. **Active site structure of holo-MmLarE**. **A** The [4Fe-4S] cluster is bound to the three conserved cysteines. An anomalous electron density map at the Fe edge, contoured at 2 σ and shown in green, is superimposed onto the active site of molecule A of holo-MmLarE. **B** In molecule A, the fourth, non-protein bonded Fe atom lies 2.1Å and 2.2 Å away from two oxygens of the phosphate group of AMP. An electron density map, omitting AMP and contoured at 2.5 σ, is shown in magenta. **C** In the other molecules in the asymmetric unit, an extra electron density near the fourth, non-protein bonded Fe atom, was attributed to a chloride ion, located 2.2 Å away from that Fe atom. The electron density map, omitting Cl^- and contoured at 2.5 σ, is shown in magenta.

A

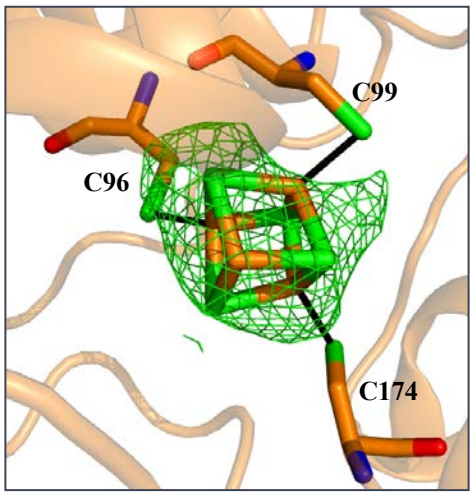

B

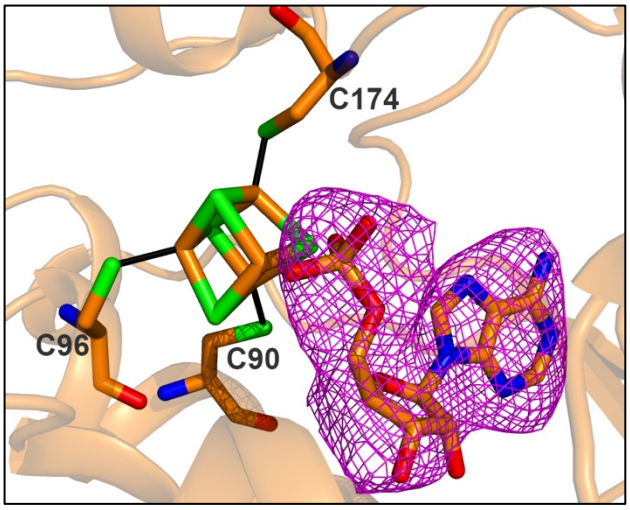

C

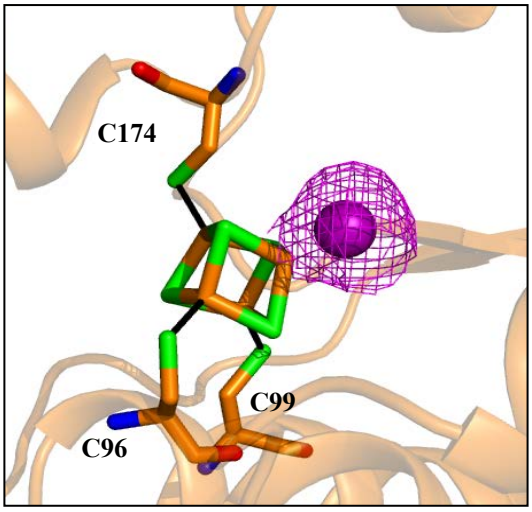

Figure 5: The apo-MmLarE structure. A Superposition of the N-terminal domains of molecules A of apo-MmLarE and holo-MmLarE with LSQ in COOT (rmsd of 1.56 Å over 156 Cα atoms). The C-terminal domains display a rotation angle of 125° and translation of 17 Å. **B**: Superposition of the N-terminal domains of molecule B of apo-MmLarE and of one monomer of holo-MmLarE (rmsd of 1.37 Å over 156 Cα atoms). The C-terminal domains display a rotation angle of 167° and translation of 27 Å. **C** Comparison of the dimers of holo-LarE (monomers in orange and green) and apo-LarE (monomers in violet and pink). **D** Zoom of the disulfide bond between CysA96 (molecule A) and CysB174 (molecule B), which links the two molecules in the asymmetric unit in apo-MmLarE. An electron density map omitting the two cysteines and contoured at 2 σ was superimposed onto the structure. **E** AMP-PNP is present in the active site of apo-MmLarE. The γ-phosphate displays two alternative conformations. An electron density map, omitting AMP-PNP and contoured at 2.5 σ, is shown in magenta.

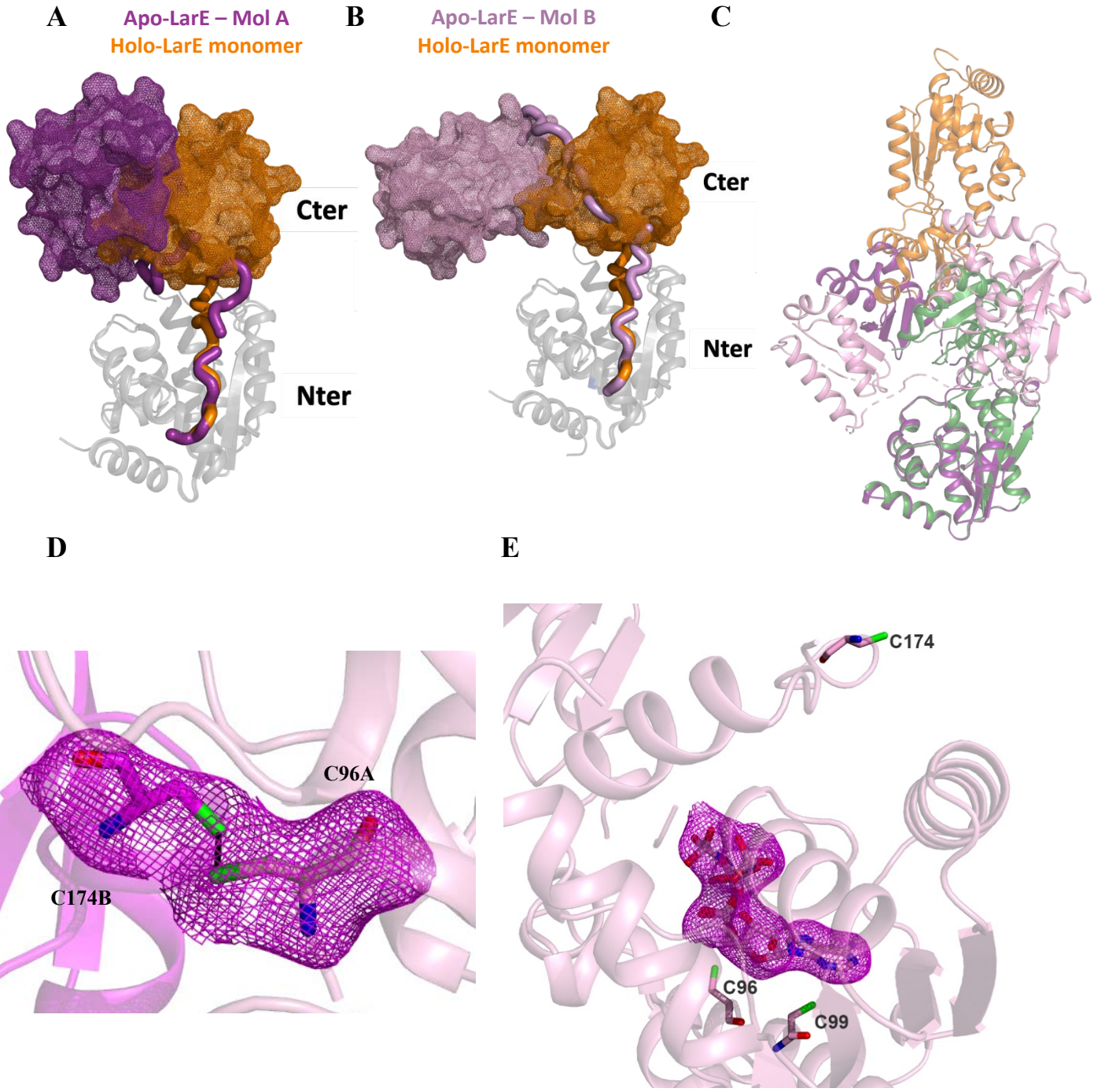

Figure 6: Comparison of the crystal structures of holo-MmLarE and LpLarE monomers. **A** Superposition of the N-terminal domains of molecule A of holo-MmLarE (in orange) in complex with AMP, and LpLarE (in blue) in complex with NMN (PDB code 5UDR, mol A) in *PYMOL*. The rmsd was 1.2 Å over 616 Cαs. The C-terminal domains of holo-MmLarE and LpLarE are shown in tan and cyan, respectively, with the linkers in yellow (MmLarE) and green (LpLarE). NMN (from the LpLarE crystal) and AMP (from the MmLarE crystal) are shown as sticks, in the same color as the domain to which they belong. The cluster of holo-MmLarE is shown in stick representation. **B** Zoom of the superposed active sites of holo-MmLarE and LpLarE. **C** Electrostatic surface of holo-MmLarE in complex with AMP (left) and LpLarE in complex with ATP and Mg^{2+} (green sphere) (PDB code 5UDS, middle) or NMN (PDB code 5UDR, right), calculated with *APBS* and colored by the electrostatic potential from red (negative) to blue (positive). The ligands and cluster are shown in stick representation. **D** Zoom of the active sites of the structures shown in (A) colored by residue conservation using *CONSURF* (Yariv et al. 2023).

A

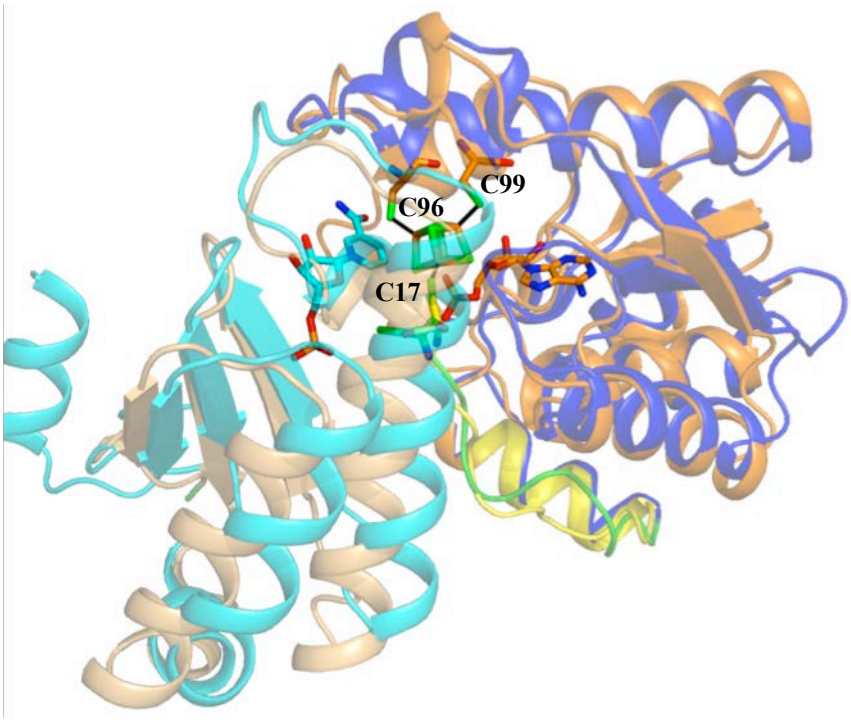

B

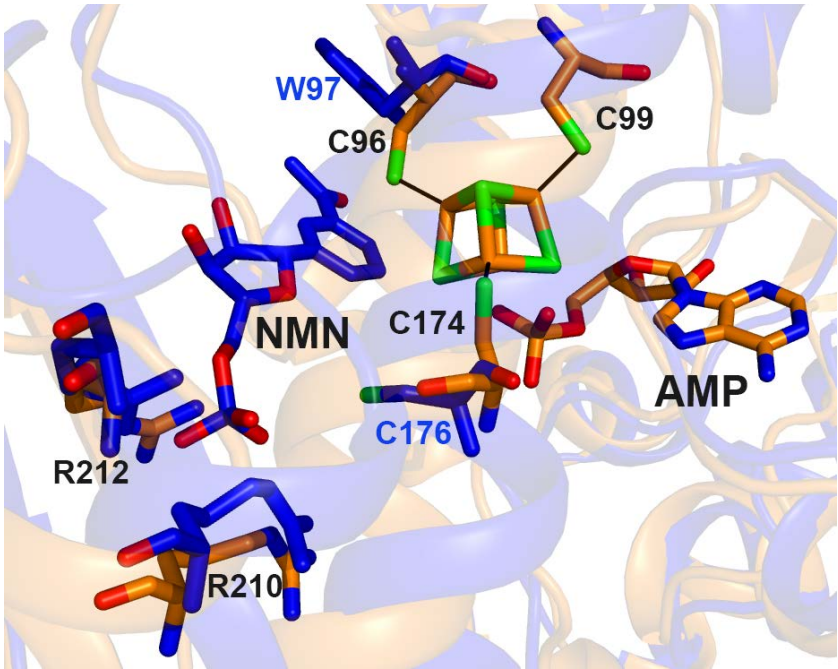

C

holo-MmLarE

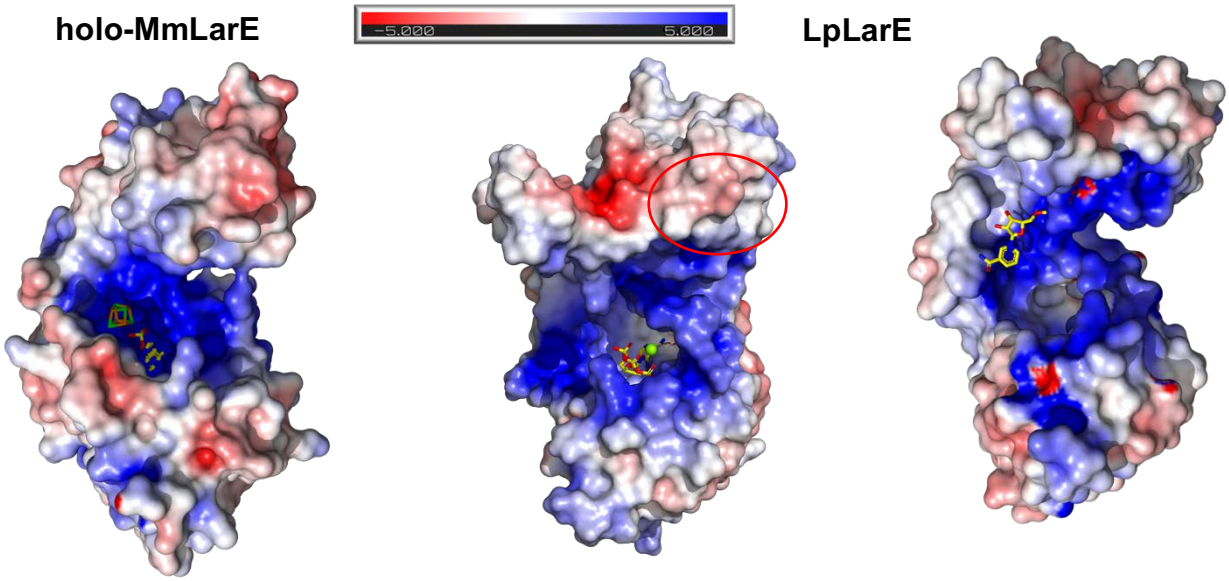

D

holo-MmLarE

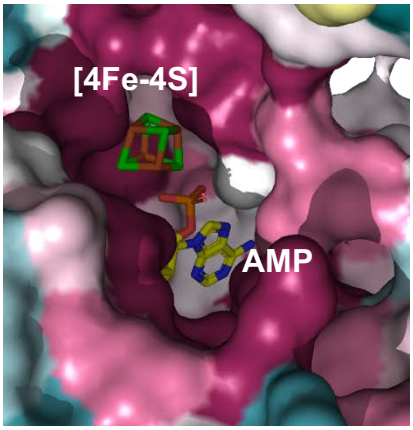

LpLarE

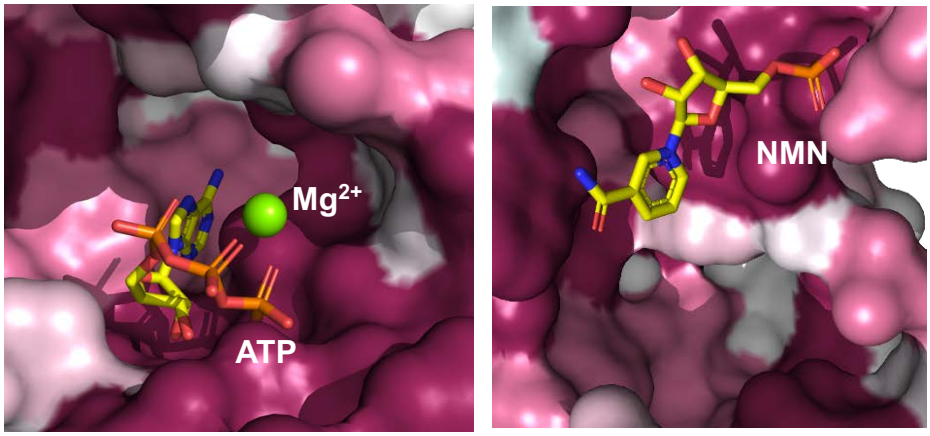

Figure 7: Catalytic mechanism and model of substrate analogue NMN bound to holo-MmLarE. **A** Proposed catalytic mechanism of ATP-dependent [4Fe-4S]-containing LarE enzymes, in which the sulfur atom attached to a [4Fe-5S] cluster intermediate is used as a sulfur donor for the thiolation reaction. This mechanism involves the formation of a P2CMN adenylate intermediate I and a tetrahedral hydrogenosulfoadenylate intermediate II. **B** Superposition of the crystal structures of holo-MmLarE (molecule B, in orange), apo-LarE in complex with AMP-PNP (in magenta) and LpLarE in complex with NMN (PDB code 5UDR, in blue) or ATP (PDB code 5UDS, in cyan). In this model of NMN bound to holo-MmLarE, the chloride atom attached to the cluster (shown as a magenta sphere), which mimics the sulfur atom used as the sulfur donor for the thiolation reaction, is located 5.4 Å away from the C4 carbon atom of the nicotinamide ring of NMN, which becomes adenylated.

A

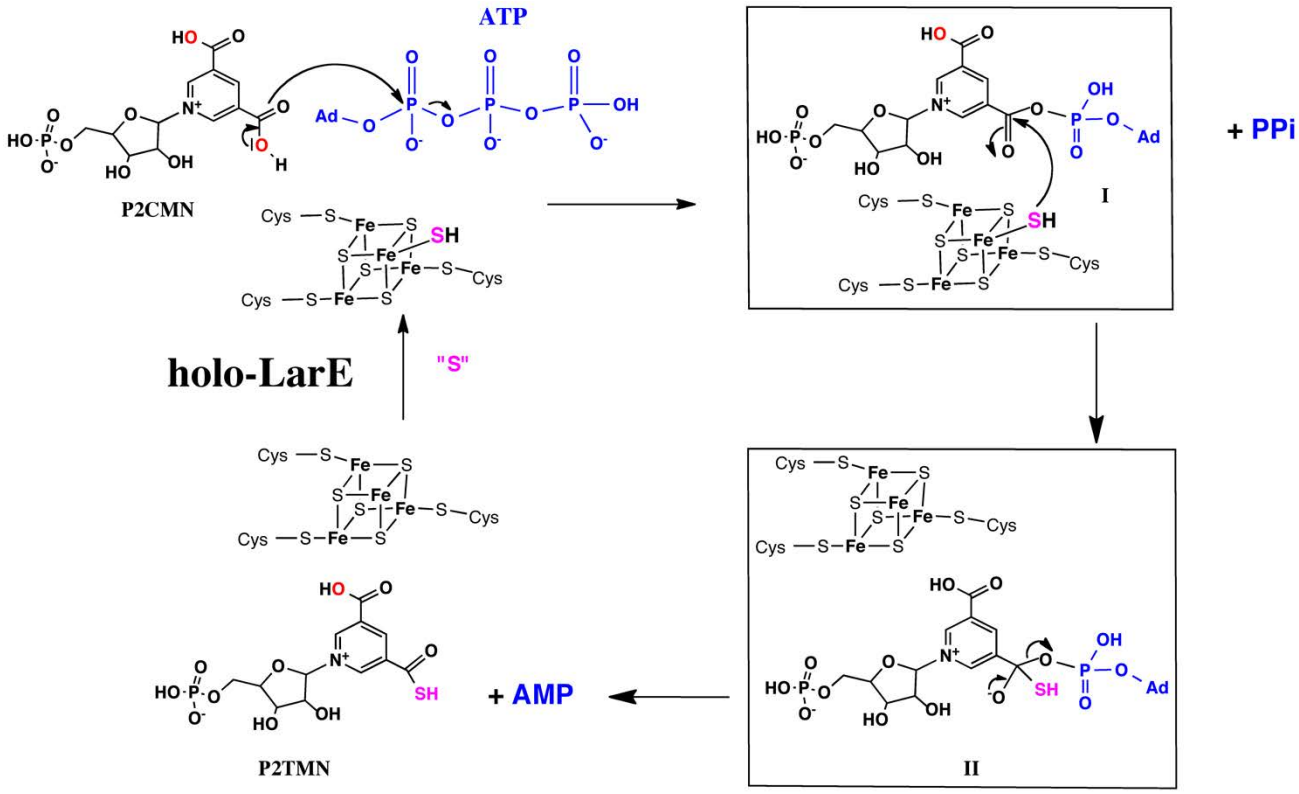

B

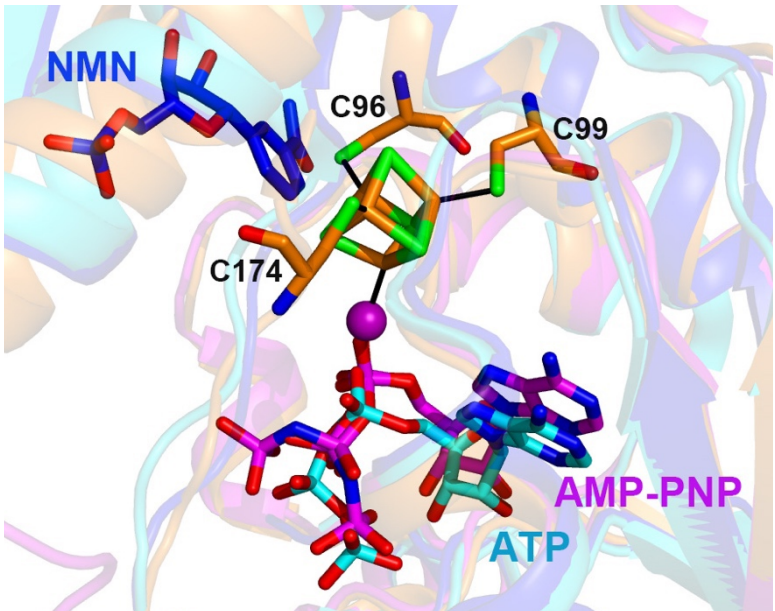

Supplementary data.

Table S1. **Mössbauer parameters of holo-MmLarE at various B and T**. Component (1) is characteristic of a $[4Fe\text{-}4S]^{2+}$ species and component (2) of nonspecifically bound high-spin Fe^{2+}.

	T = 77.0 K B_{ext} = 0.0 T				T = 4.2 K B_{ext} = 0.1 T	T = 4.2 K B_{ext} = 5.0 T
δ (mm s^{-1})	0.43	(1)	1.13	(2)	0.43 (1)	0.43 (1)
ΔE_Q (mm s^{-1})	1.14	(1)	2.69	(2)	1.14 (1)	1.14 (1)
Γ (mm s^{-1})	0.35	(1)	0.30	(2)	0.41 (1)	0.35 (1)
η						0.8 ± 0.1
Area (%)	97	(1)	3	(2)	100	100

Table S2. Comparison of the monomers of the holo-MmLarE crystal structure and the AlphaFold model. The Cα traces of the 7 molecules in the asymmetric unit of the holo-MmLarE structure used for phasing and that of the AlphaFold model (AF) were superimposed with ProFitv3 (http://www.bioinf.org.uk/software/profit/). The RMSD over 248 aligned Cαs is indicated in Å.

	AF	Chain A	Chain B	Chain C	Chain D	Chain E	Chain F	Chain G
AF	-	0.572	0.829	0.871	0.816	0.752	0.583	0.598
Chain A		-	0.751	0.759	0.743	0.623	0.4	0.4
Chain B			-	0.416	0.36	0.315	0.638	0.541
Chain C				-	0.3	0.363	0.701	0.643
Chain D					-	0.317	0.689	0.642
Chain E						-	0.59	0.474
Chain F							-	0.394
Chain G								-

Figure S1. Sequence alignment of several LarE proteins. Amino acid sequence alignment of several LarE proteins (MmLarE, *Thermotoga maritima*, WP_004080596.1; *Thermoanaerobacter thermosaccharolyticum*, WP_094046537.1; *Clostridium homopropionicum*, WP_175478652.1; *Staphylococcus epidermidis*, WP_038812312.1; *Enterococcus faecalis*, WP_033597706.1; *Bacilli bacterium*, genbank PZD88032.1, LpLarE) was performed with CLUSTAL Omega (Sievers et al. 2011) and rendered with ESPript (Gouet et al. 1999). The secondary structure elements of MmLarE and LpLarE, which have been structurally characterized, are shown at the top and bottom of the alignment, respectively. The cysteines of MmLarE involved in iron-sulfur cluster coordination are shown as blue dots, above the alignment whereas the sacrificial cysteine of LpLarE is shown as a magenta dot, below the alignment.

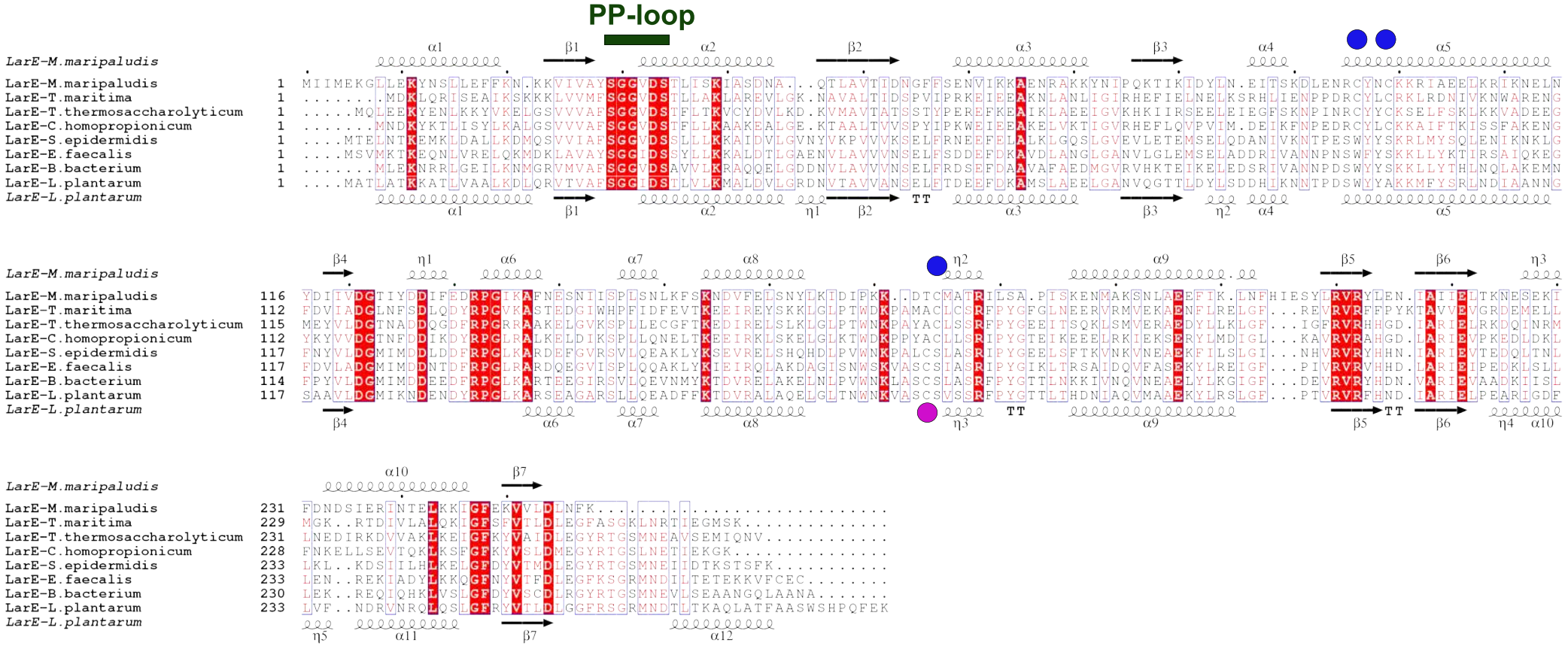

Figure S2. Purification of apo-MmLarE. A Nickel affinity chromatography of 'as-purified' MmLarE. The absorbance at 280 nm and 410 nm are shown as full and dashed lines, respectively. **B** Purification of 'as-purified' MmLarE by size exclusion chromatography on a Superdex 75 gel 16/60 filtration column. **C** 14 % SDS PAGE gel of 'as-purified' MmLarE (1) and holo-MmLarE (2).

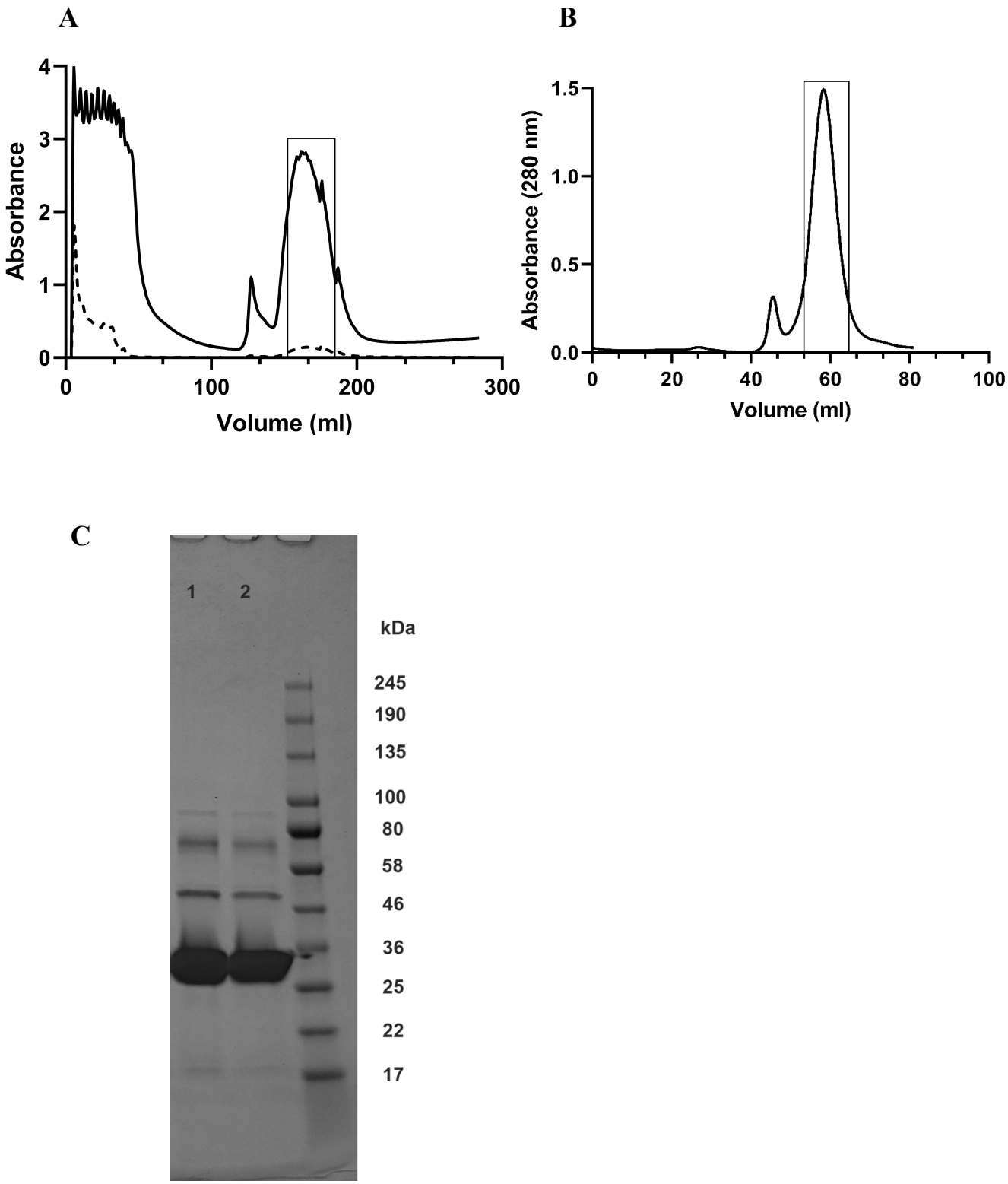

Figure S3. **Purification and determination of molar mass of holo-MmLarE**. **A** Purification of holo-MmLarE by size exclusion chromatography on a Superdex 200 gel filtration column. **B** SEC-MALS analysis of holo-MmLarE. dRI is the differential refractive index.

A

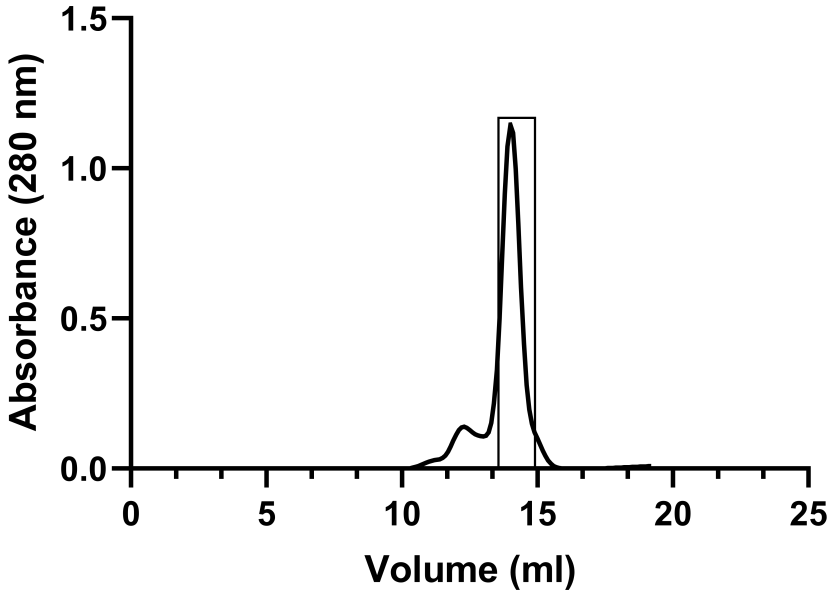

B

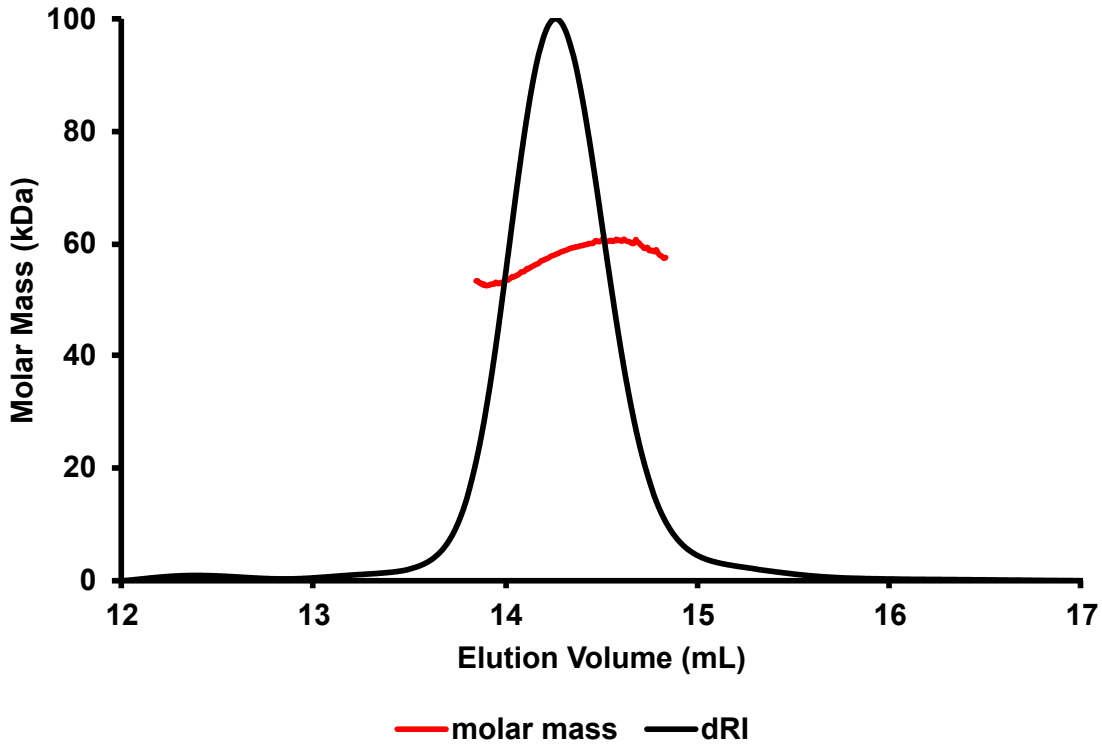

Figure S4. **Mössbauer spectra of holo-MmLarE** (540 µM) in 50 mM TRIS-HCl pH 8.5, 180 mM NaCl, 5 mM DTT. **A**. T=4.2K, B_{ext}=0.1T. **B** T=4.2K, B_{ext}=5T. Solid lines are simulations with the parameters given in Table S1.

A

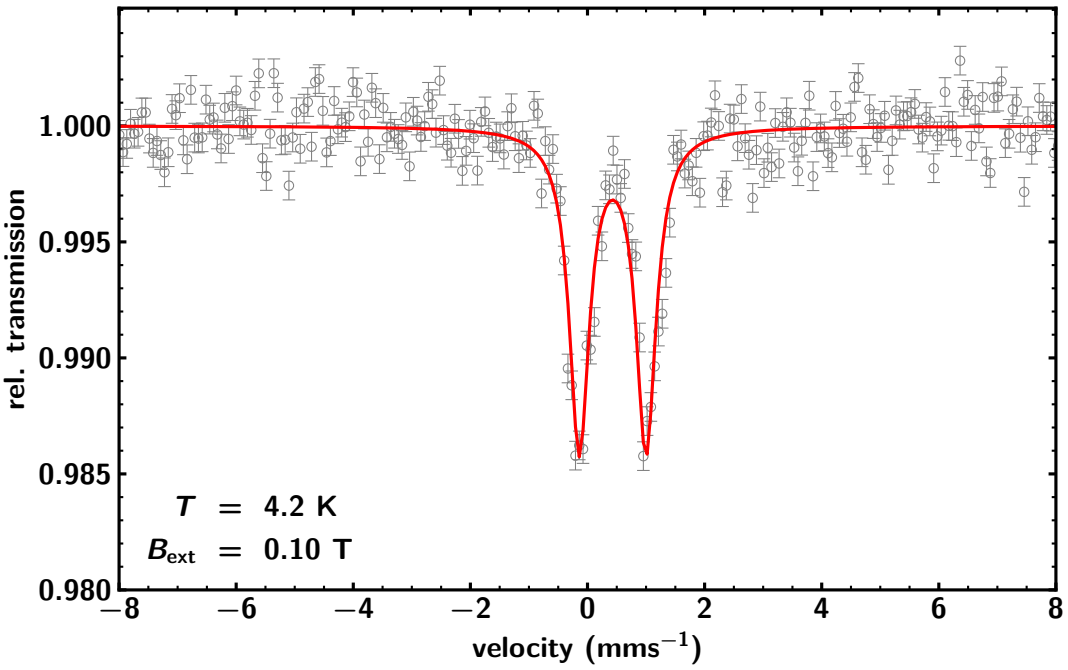

B

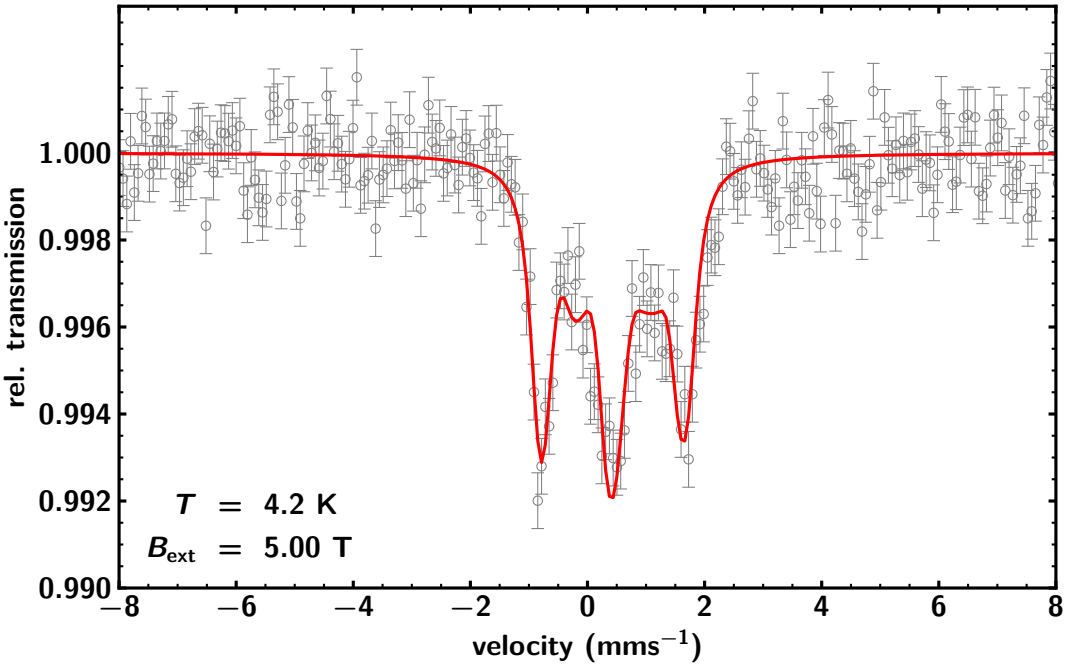

Figure S5: Stereo view of the crystal packing of holo-MmLarE involving heptamers of dimers.

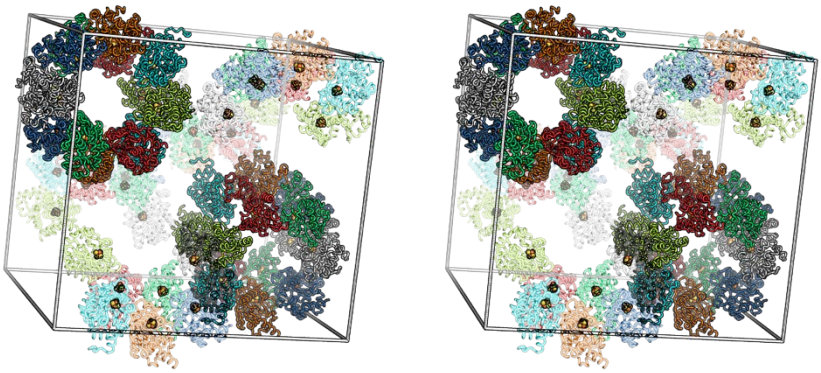

Figure S6. Comparison of the holo-MmLarE crystal structure and the AlphaFold model. **A** AlphaFold model in two orthogonal views, with the conserved cysteines in stick representation. **B** Same views of the superposition of the seven molecules in the asymmetric unit of holo-MmLarE with the AlphaFold model. The colors of the monomers are limon (A), tv_red (B), limegreen (C), cyan (D), orange (E), white (F), skyblue (G), forest (AlphaFold). **C** Comparison of the dimers of the holo-MmLarE crystal structure (in green and orange) and AlphaFold model (in magenta and pink) after superposition of one monomer (in green and magenta).

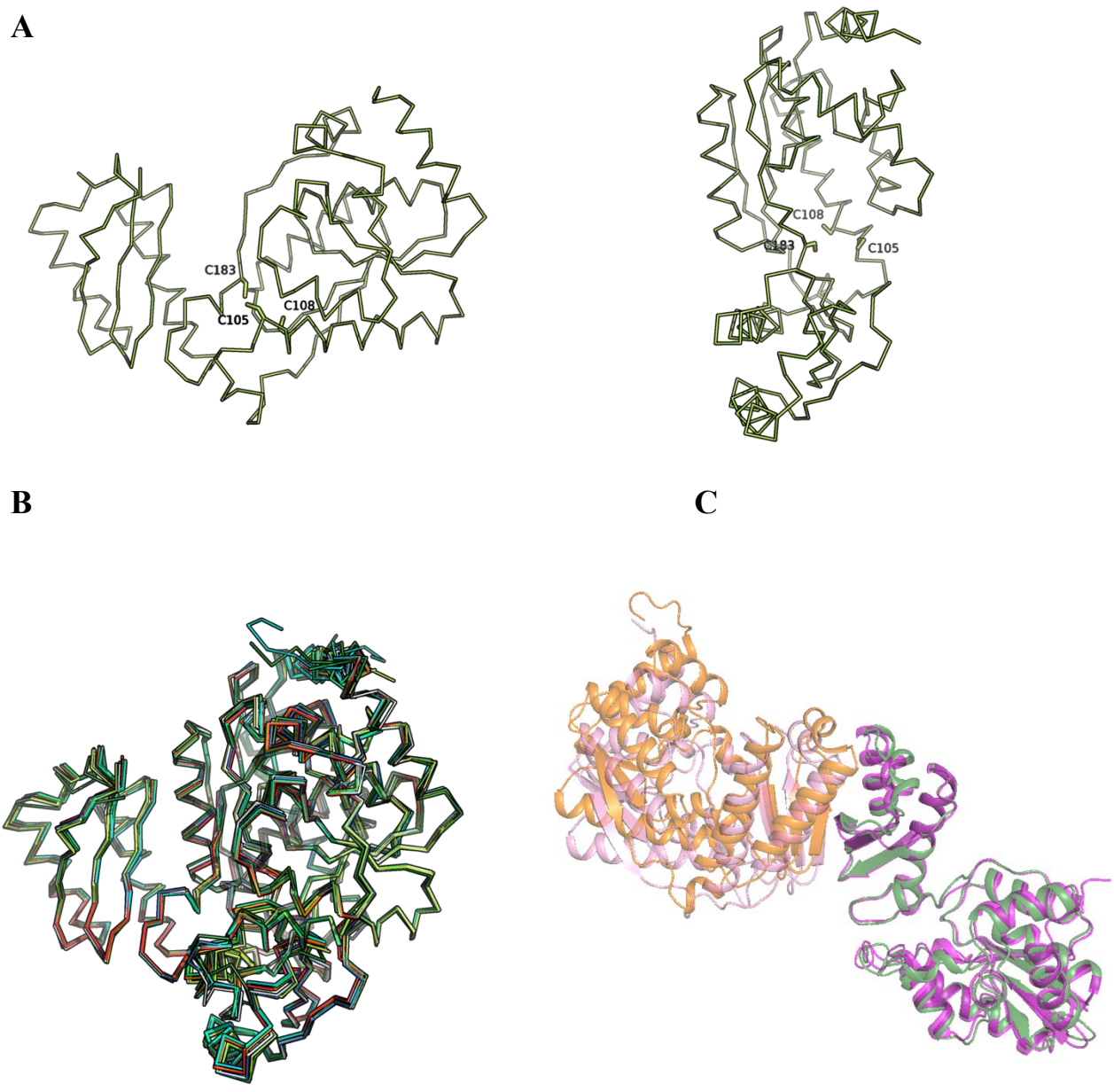

Figure S7: Analysis of small molecule content in as-purified MmLarE. A Reversed-phase HPLC analysis of nucleotide co-purified with MmLarE. Top: AMP standard, middle: ATP standard, bottom: LarE sample. The HPLC chromatogram is shown on the left and the absorption spectrum on the right. **B** Nano-LC-MS analysis of 'as-purified' MmLarE in 50 mM Tris pH 8.5, 300 mM NaCl, 5 mM 2-b-mercaptoethanol. The deconvoluted spectrum is shown.

A

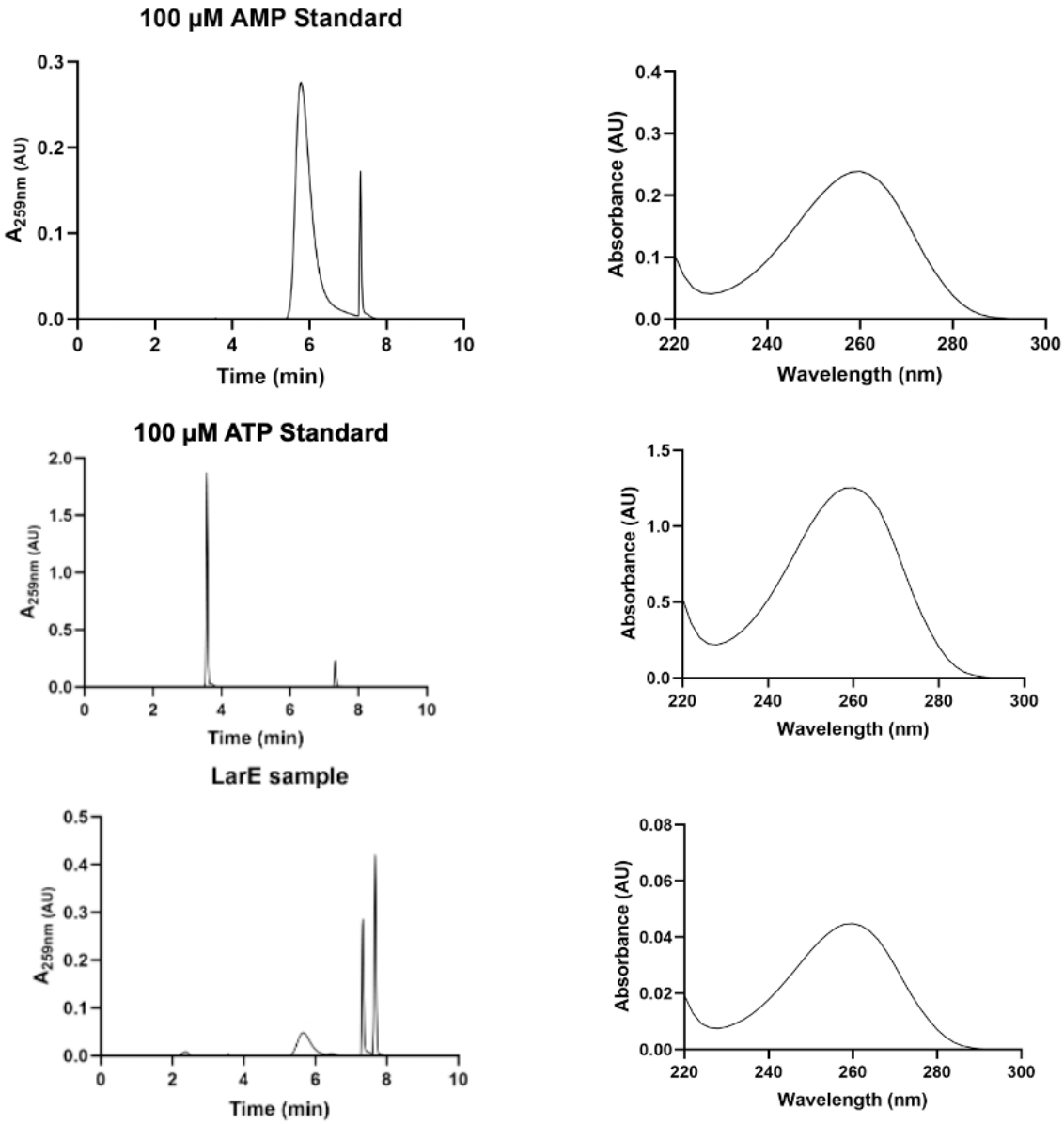

B

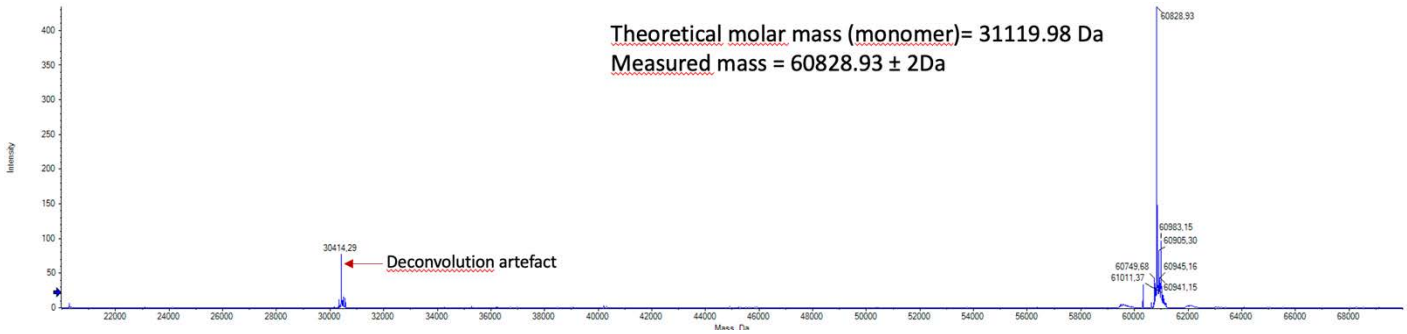

Figure S8: Thermal motions in the apo-MmLarE and holo-MmLarE crystal structures. **A** Comparison of the B-factors for the two molecules in apo-MmLarE. **B** Crystal packing of apo-MmLarE, with the B-factors in putty representation, the radius being proportional to the B-factor (chain A in blue and chain B in orange). The C-terminus of chain B is indicated by an arrow. The higher disorder in the C-terminal domains, compared to the N-terminal domains, is clearly shown by the increased radius. **C** B-factors in holo-MmLarE.

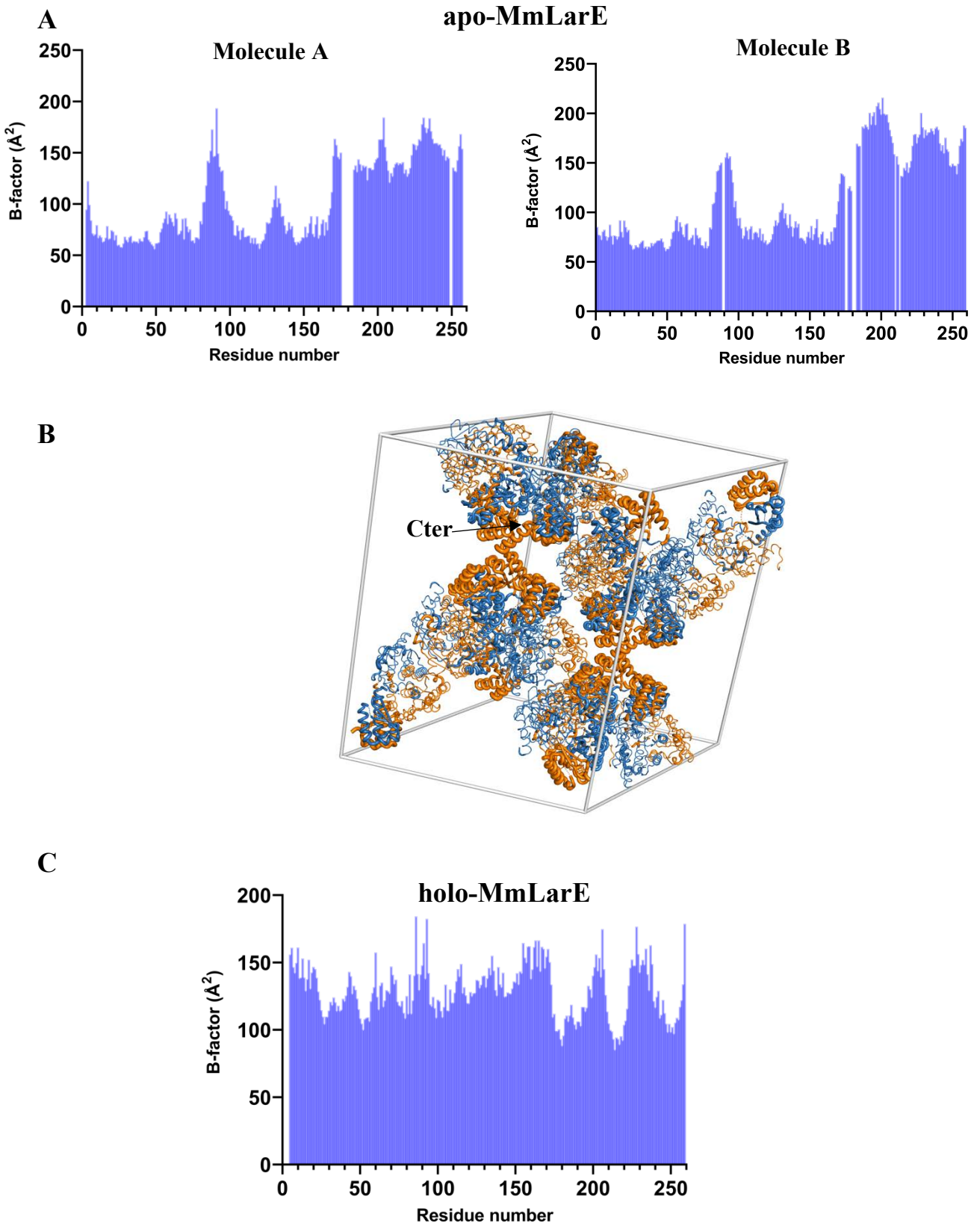

Figure S9: Structure of LpLarE bound to NMN. A Comparison of the structures of the P2CMN substrate and NMN. **B** LigPlot analysis of NMN bound to LpLarE (PDB code 5UDR, molecule A).

A

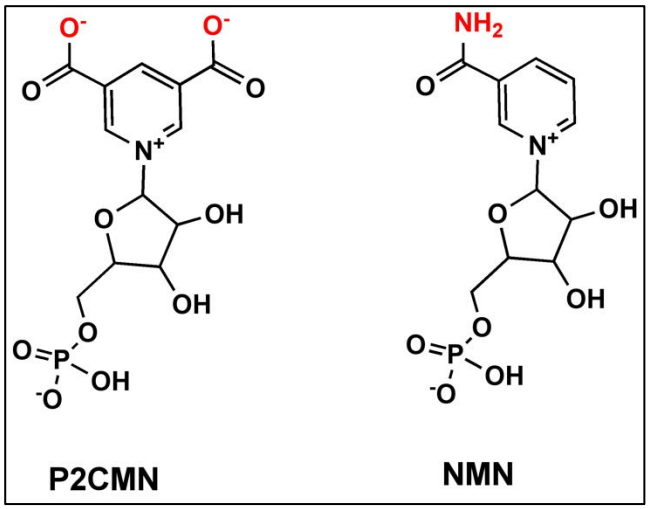

B

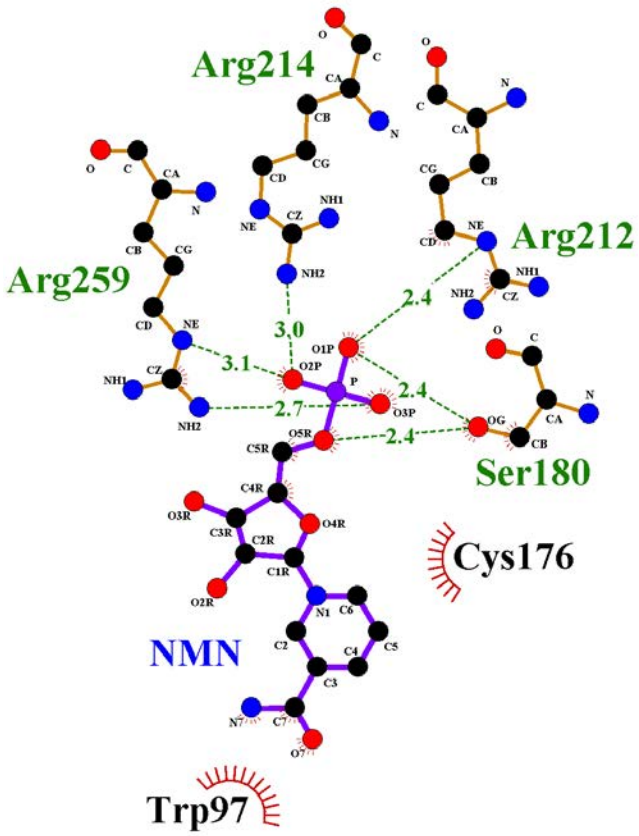

Figure S10: Comparison of the nucleotide binding sites of MmLarE and LpLarE. **A** LigPlot analysis of the residues involved in binding AMP in holo-MmLarE (chain A), AMP-PNP in apo-MmLarE (chain A), ATP in LpLarE (PDB code 5UDS, chain A) and AMP in LpLarE (PDB code 5UDT, chain A). The loop containing Arg133 is disordered in the LpLarE/ATP complex. **B** Superposition of the active site structures of apo-MmLarE bound to AMP-PNP and LpLarE bound to ATP (RMSD of 1.64 Å over 157 Cα atoms). **C** Superposition of the active site structures of holo-MmLarE bound to AMP and LpLarE bound to AMP (same orientation as in (**B**) (RMSD of 1.75 Å over 226 Cα atoms).

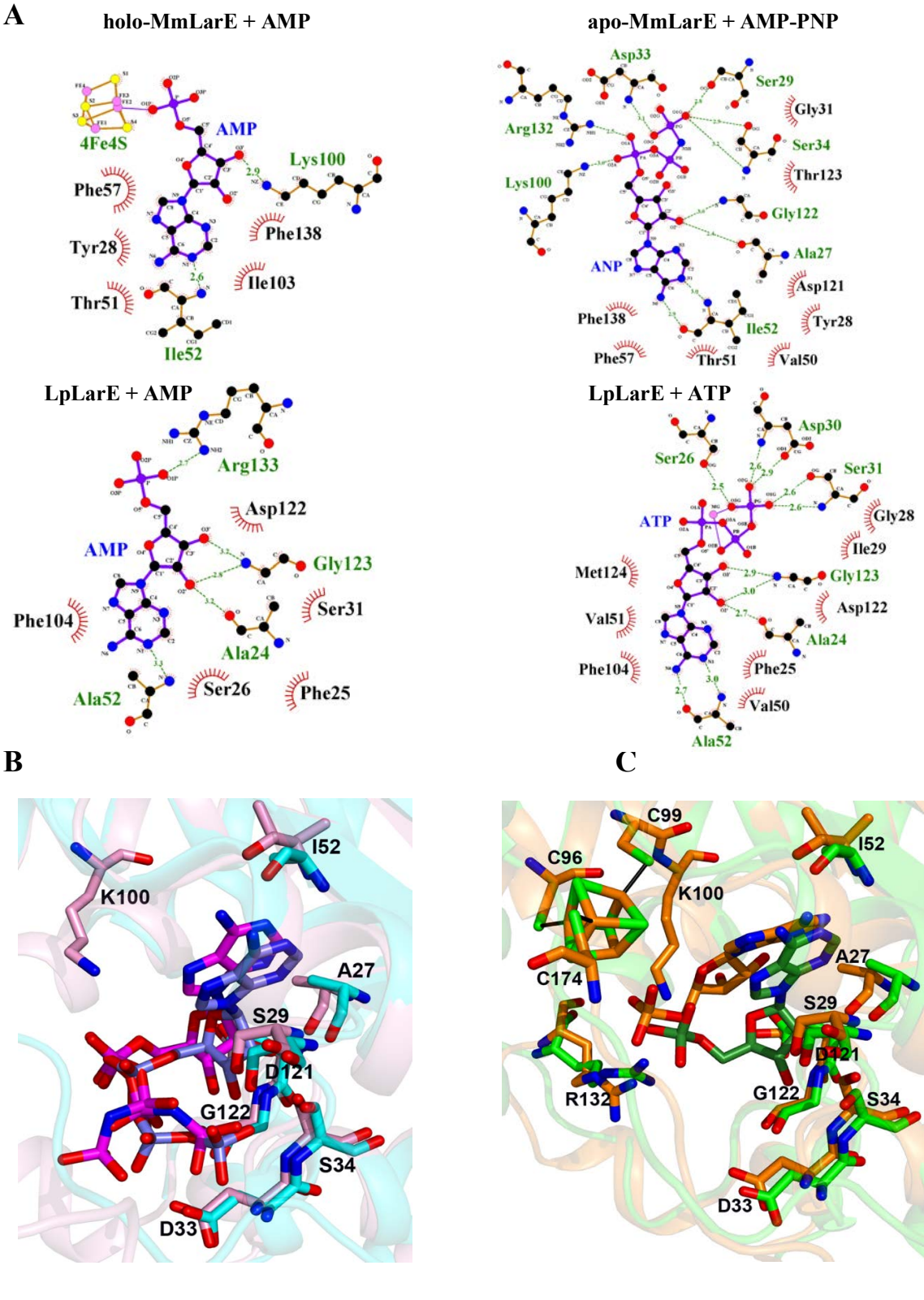

Figure S11. Models of the main catalytic intermediates along the MmLarE-catalyzed-reaction. See Material and Methods for details about the modeling. **A** Model of holo-MmLarE in complex with ATP and P2CMN based on the superposition of the crystal structures, as depicted in Figure 7B. **B** LigPlot analysis of the manual models of the main intermediates along the first sulfur insertion reaction catalyzed by MmLarE (see Figure 7A).

A

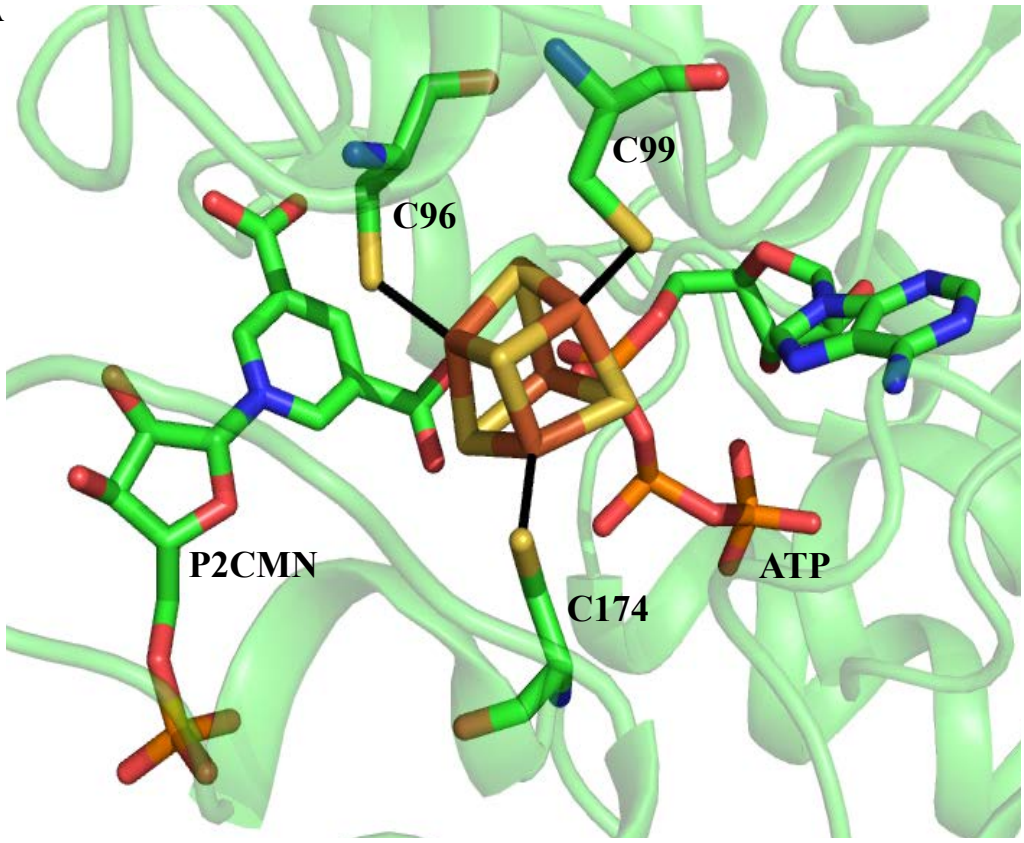

B

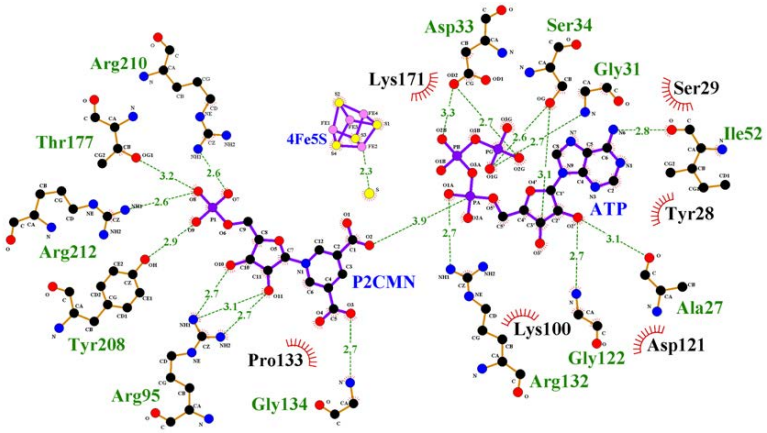
Asp33
Ser34
Arg210
Lys171
Gly31
Ser29
Thr177
4Fe5S
Ile52
ATP
Tyr28
Arg212
P2CMN
Ala27
Tyr208
Lys100
Asp121
Pro133
Gly122
Arg132
Arg95
Gly134

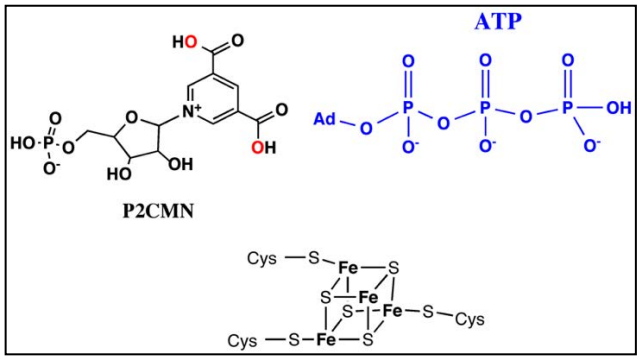
ATP
P2CMN
Cys
Fe
S
Cys

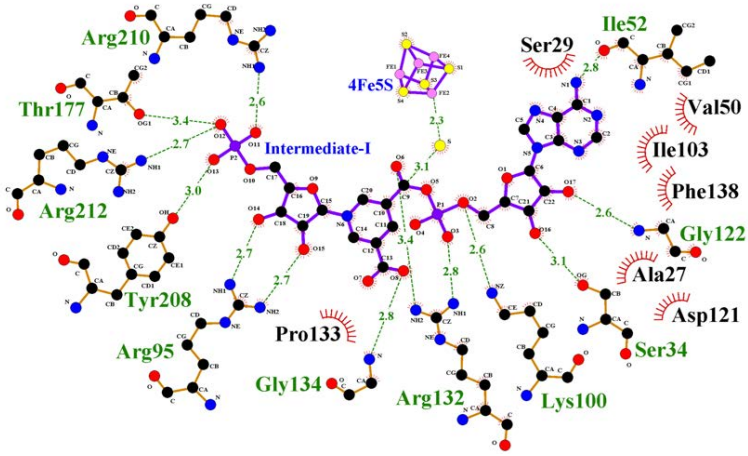
Arg210
Ile52
Ser29
4Fe5S
Thr177
Val50
Intermediate-I
Ile103
Phe138
Arg212
Gly122
Ala27
Tyr208
Asp121
Pro133
Ser34
Arg95
Gly134
Arg132
Lys100

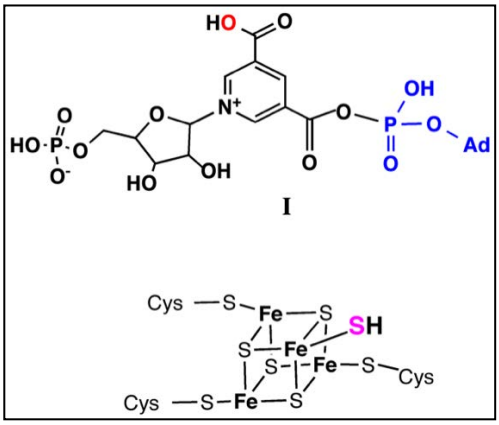
I
SH
Cys
Fe
S
Cys

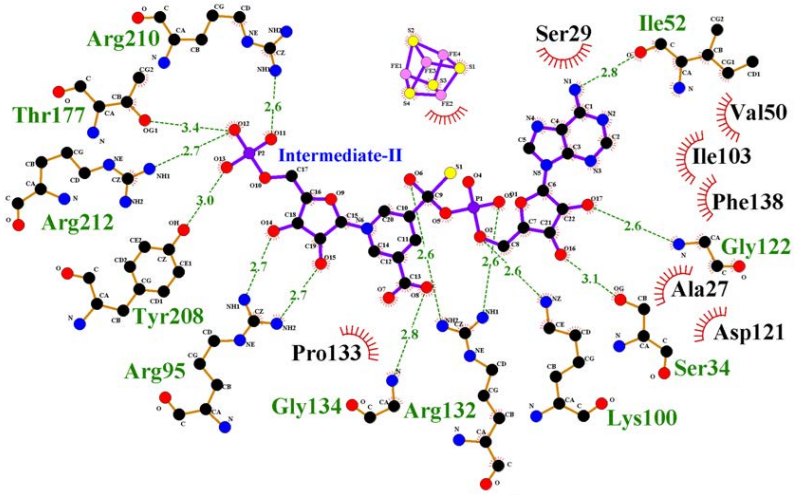
Arg210
Ser29
Ile52
Thr177
Val50
Intermediate-II
Ile103
Phe138
Arg212
Gly122
Ala27
Tyr208
Asp121
Pro133
Ser34
Arg95
Gly134
Arg132
Lys100

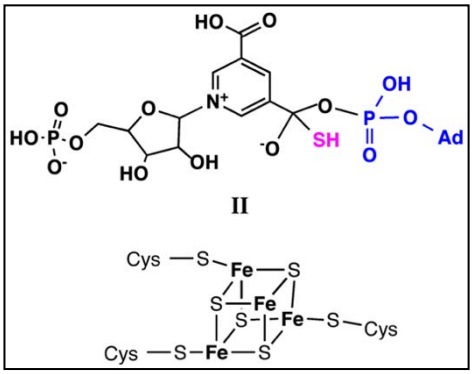
II
SH
Cys
Fe
S
Cys

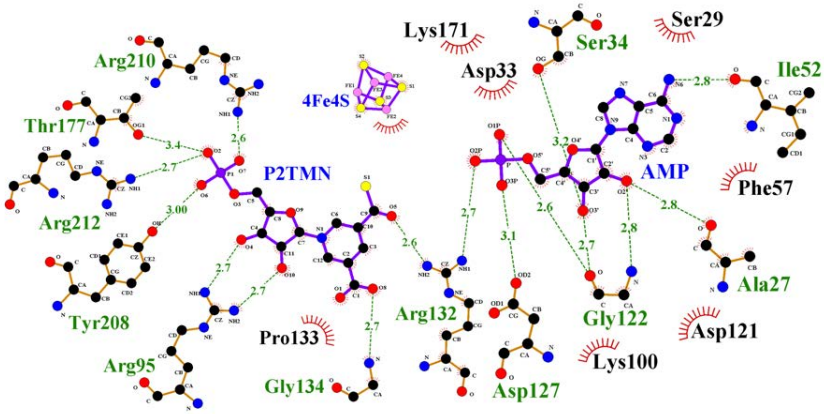
Lys171
Ser29
Ser34
Arg210
Asp33
Ile52
4Fe4S
Thr177
AMP
P2TMN
Phe57
Arg212
Ala27
Tyr208
Arg132
Gly122
Asp121
Pro133
Lys100
Arg95
Asp127
Gly134

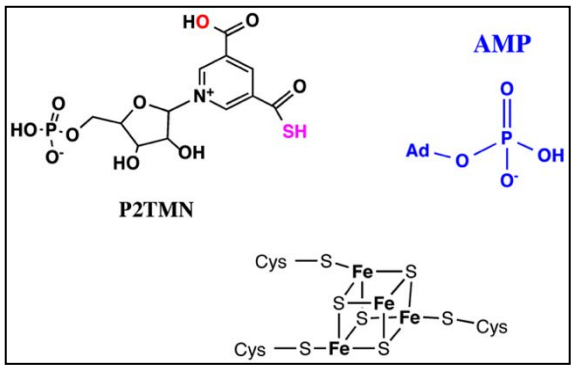
AMP
P2TMN
SH
Cys
Fe
S
Cys

Figure S12. LigPlot analysis of models of the main intermediates along the sulfur insertion reaction catalyzed by LpLarE. The models have been generated based on the crystal structures, as described for the MmLarE intermediates in Material and Methods. DHA stands for 'dehydroalanine'.

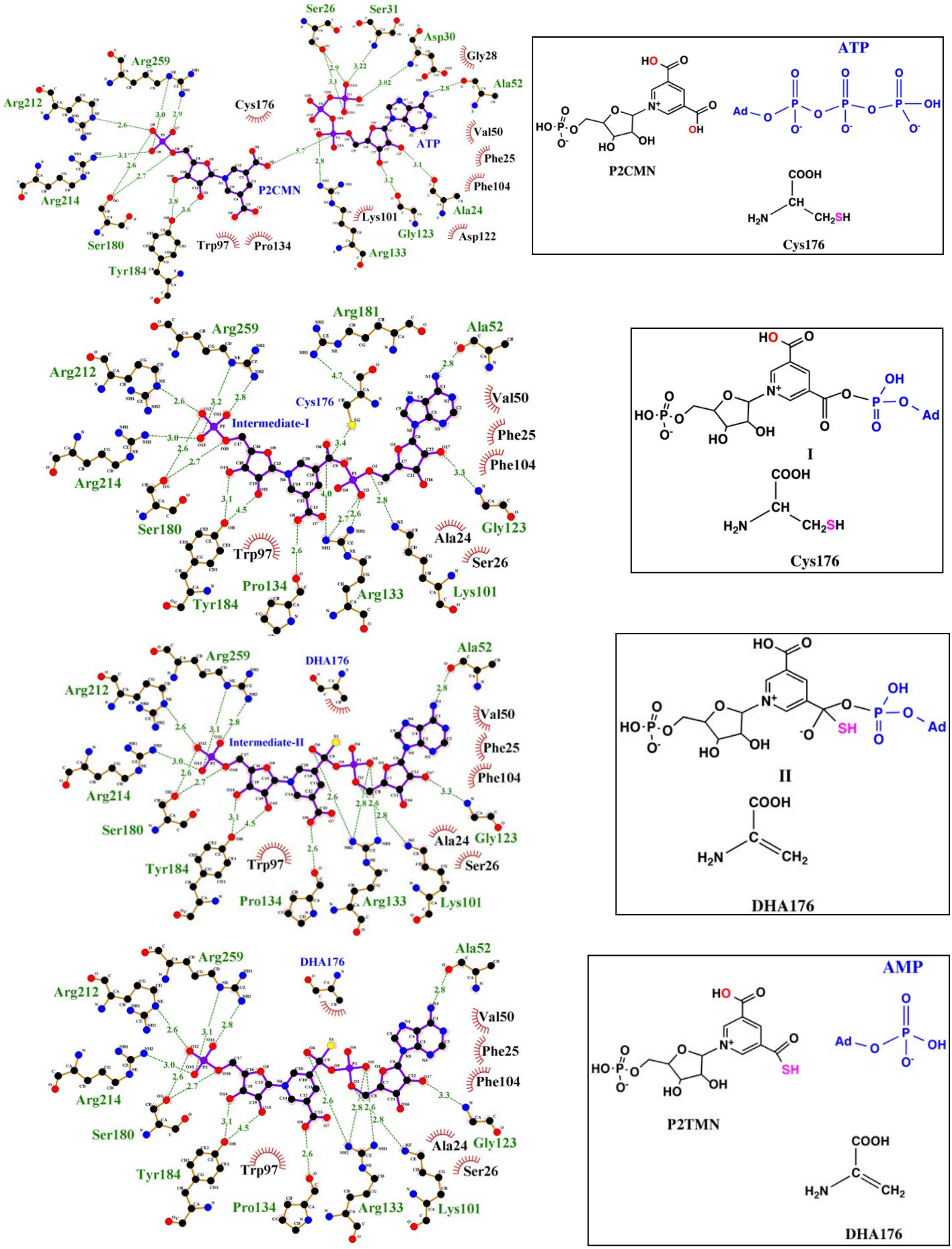

Figure S13. Comparison of the residues conservation between MmLarE (A) and LpLarE (B). The mmseq2 alignment obtained with Colabfold (https://colab.research.google.com/github/sokrypton/ColabFold/blob/main/AlphaFold2) was filtered with *HHFilter* (Gabler et al. 2020) using the following parameters: Min Id: 50% Min Cov 65% Max Id 95%. The resulting alignment was rendered with WebLogo (Bogdan et al. 2001).

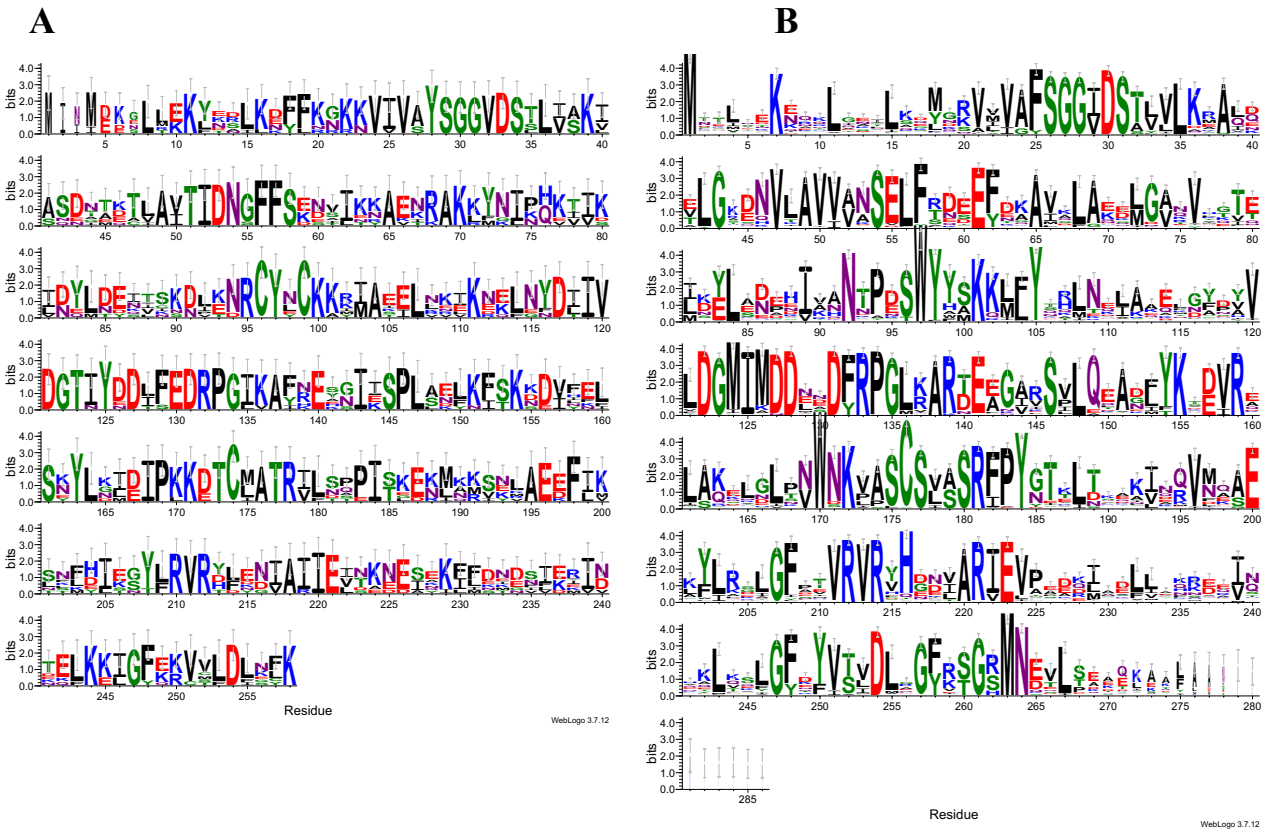

References

Bogdan, J.A., Nazariolarrieu, J., Sarwar, J., Alexander, P., and Blake, M.S. 2001. *Bordetella pertussis* autoregulates pertussis toxin production through the metabolism of cysteine. *Infect Immun* **69**: 6823.

Gabler, F., Nam, S.Z., Till, S., Mirdita, M., Steinegger, M., Söding, J., Lupas, A.N., and Alva, V. 2020. Protein Sequence Analysis Using the MPI Bioinformatics Toolkit. *Curr Protoc Bioinformatics* **72**(1): e108.

Gouet, P., Courcelle, E., Stuart, D.I., and Metoz, F. 1999. ESPript: analysis of multiple sequence alignments in PostScript. *Bioinformatics* **15**(4): 305-308.

Sievers, F., Wilm, A., Dineen, D., Gibson, T.J., Karplus, K., Li, W., Lopez, R., McWilliam, H., Remmert, M., Soding, J. et al. 2011. Fast, scalable generation of high-quality protein multiple sequence alignments using Clustal Omega. *Mol Syst Biol* **7**: 539.